Ceramics International 50 (2024) 25080–25094

Contents lists available at ScienceDirect

Ceramics International

journal homepage: www.elsevier.com/locate/ceramint

Synergistic enhancement of simazine degradation using ZnO nanosheets and ZnO/GO nanocomposites: A sol-gel synthesis approach

Sakir Aydogan [a,b], Nurtac Canpolat [c], Adem Kocyigit [d], Mehmet Yilmaz [b,e,*]

[a] Department of Physics, Faculty of Sciences, Ataturk University, Erzurum, Turkey
[b] Advanced Materials Research Laboratory, Department of Nanoscience and Nanoengineering, Graduate School of Natural and Applied Sciences, Ataturk University, Erzurum, Turkey
[c] Department of Chemistry, K. K. Education Faculty, Ataturk University, Erzurum, Turkey
[d] Department of Electronics and Automation, Vocational High School, Bilecik Seyh Edebali University, Bilecik, Turkey
[e] Department of Science Teaching, K. K. Education Faculty, Ataturk University, Erzurum, Turkey

ARTICLE INFO

Handling Editor: Dr P. Vincenzini

Keywords:
ZnO
Sol–gel processes
Nanocomposites

ABSTRACT

This study aims to optimize the synergistic effect in photocatalytic processes by facilitating the accumulation of graphene oxide (GO) layers onto ZnO nanoparticles, thereby achieving close contact between the two materials, leveraging the high surface-to-volume ratio and efficient charge transport pathways inherent in ZnO nanosheets. The performance of ZnO nanosheets in the photocatalytic degradation of Simazine was investigated, with the aim of further enhancing the performance of the best-performing sample through GO decoration. Accordingly, ZnO nanosheets were obtained by the sol-gel method using different concentration of zinc acetate hexahydrate as a zinc source. According to the obtained results, it was observed that the sample prepared with a concentration of 0.44 M zinc precursor salt exhibited the best performance with a degradation rate of 67 %. In order to improve the performance of the sample prepared under this condition, graphene oxide (GO) was integrated into ZnO nanosheets to form a ZnO/GO nanocomposite structure. This composite structure achieved a photodegradation efficiency of 85 % for Simazine. The data obtained showed that the use of GO-based ZnO nanocomposites can improve charge separation, light absorption, charge transport and photo-oxidation of organic pollutants.

1. Introduction

Due to the development of industrialization to meet the needs of a growing population, pesticides are being detected more frequently in the environment, and this causes a threat to public health [1,2]. Although the concentration of these pesticides is low in the aquatic environment (from ng L^{-1} to μg L^{-1}), they pose a hazard due to their high stability and bio-accumulative properties. For example, simazine, a kind of herbicide that can be considered in the category of pesticides, can remain in the soil for up to 149 days and traces of simazine have been found in rivers during its widespread usage [3]. According to the literature, simazine, which has been widely used in the last 50 years, has been detected in the natural environments of Asia, Europe, Australia, and America, and it can lead to endocrine disruption in living organisms even at low concentrations [4]. Therefore, researchers have recently accelerated their efforts to develop effective purification methods for the removal and detoxification of this herbicide from clean groundwater sources. Among these efforts, various treatment methods are commonly employed, including chemical precipitation [5], separation [6], adsorption [7], coagulation [8], biological treatment [9], and Fenton oxidation [10] techniques etc … Each of these mentioned techniques has both advantages and disadvantages. For instance, chlorination oxidation, while capable of removing up to 60 % of the studied pesticides, can lead to the formation of trihalomethanes to make the liquid useful [11]. However, these methods suffer from their inherent problems of inefficiency or high costs. The use of metal-semiconductor composites as photocatalyst for degradation of these pollutants present a solution as an alternative [12].

Photocatalytic degradation can be seen as an efficient and energy-saving method to be used for the removal of triazines, a class of nitrogen-containing heterocycles, from water resources [13]. On the

* Corresponding author. Advanced Materials Research Laboratory, Department of Nanoscience and Nanoengineering, Graduate School of Natural and Applied Sciences, Ataturk University, Erzurum, Turkey.
E-mail addresses: saydogan@atauni.edu.tr (S. Aydogan), nurtac@atauni.edu.tr (N. Canpolat), adem.kocyigit@bilecik.edu.tr (A. Kocyigit), mehmetyilmaz@atauni.edu.tr, yilmazmehmet32@gmail.com (M. Yilmaz).

https://doi.org/10.1016/j.ceramint.2024.04.236
Received 22 February 2024; Received in revised form 8 April 2024; Accepted 18 April 2024
Available online 25 April 2024

other hand, photocatalysis aims to remove pollutants by breaking the bonds of pollutant molecules through the interaction between the catalyst and adsorbed pollutant molecules by producing reactive oxygen species (ROS) through surface reactions [14,15]. The use of metal-semiconductor nanocomposites as photocatalysts for the degradation of these pollutants may offer a solution to increase the efficiency of photocatalytic process with a potential synergistic effect. In recent years, researches have focused on the hybridization of inorganic nanomaterials with other materials to improve photocatalytic performance for promising results [16,17]. These efforts are generally aimed at reducing exciton recombination and thus increasing the production of additional ROS [18,19]. In this context, ZnO nanoparticles with a hexagonal wurtzite crystal structure and special defect chemistry exhibit significant states in the band gap energy, which enables photocatalysis under UV light [20,21]. However, despite these properties and the large direct bandgap of 3.37 eV, the photocatalytic activity of ZnO nanoparticles was reported to be very low due to the high recombination rate of photo-generated excitons (electron-hole pairs) and poor adsorption capacity [22]. For this purpose, as mentioned above, new attempts are being made on ZnO-based photocatalysts from doping to obtaining new composites [23]. For instance, Adabavazeh et al. [24]. have investigated the photocatalytic performance of PANI/ZnO–$CoMoO_4$ nanocomposite and, they have leveraged the potential of PANI composites to create a p-n heterojunction electric field at the interface with a n-type semiconductor. Utilizing this electric field, they observed rapid transfer of photo-generated holes to PANI, facilitating the oxidation of surrounding species. Additionally, they have concluded that photo-generated electrons are swiftly transferred to the n-type semiconductor composite, inducing reduction reactions on its surface, thereby demonstrating its potential as a highly efficient catalyst. Additionally, carbon-based materials, including carbon dots, GO and r-GO, have sp2/sp3 carbon and carboxyl or hydroxyl groups. Due to their unique properties, these materials have a wide range of applications [25]. In the study [26], the aim was to increase the electron-hole recombination time in TiO_2-rGO nano-composites. They demonstrated that both the hybridized HBK-rGO and P25-rGO were effective in the removal of a pesticide mixture using O_2 and H_2O_2 as oxidants. Recently, there has been a significant focus on studying the synergistic effects that can arise from the combination of graphene oxide (GO) with other semiconductor materials, particularly regarding their electrical conductivity and charge separation capabilities, and GO-based nanocomposites exhibit notable characteristics in photocatalytic processes [27–30]. Essentially, it is anticipated that to compose with GO may vary depending on the specific application under investigation. Since, ZnO has direct bandgap, 60 MeV exciton binding energy, corrosion resistance, non-toxic nature, and ability to adsorb and degrade toxic organic compounds, investigation the degradation performance of ZnO/GO nanocomposites is significant [31]. Furthermore, specific ZnO nanostructures with nanosheets geometry have been synthesized within the scope of this study due to their desired advantages such as enhanced surface area, improved charge transfer, and adjustable characteristics for photocatalytic applications. Additionally, GO has a lower work function than ZnO [32], it prevents recombination losses in photocatalytic processes by clearing the excited electron from the conduction band of ZnO. As a result of all these discussions, in the present study, considering the potential of graphene oxide layers as excellent electron acceptors due to their large surface area, ZnO nanosheets have been decorated with GO layers as an alternative to the catalysts mentioned in the literature. In summary, this study aims to optimize the synergistic effect in photocatalytic processes by facilitating the accumulation of graphene oxide (GO) layers onto ZnO nanoparticles, thereby achieving close contact between the two materials, leveraging the high surface-to-volume ratio and efficient charge transport pathways inherent in ZnO nanosheets, as mentioned earlier.

2. Experimental

ZnO nanosheets were obtained by the sol-gel method using zinc acetate hexahydrate as a zinc source. In summary, zinc salt was dissolved in 50 mL of ethanol at 60 °C to achieve concentrations of 0.40, 0.42, 0.44, and 0.46 M. For this purpose, 3 drops of HCl were added to each solution, resulting in the formation of a transparent solution. Dilute NaOH solution was added as dropwise into solutions to increase the pH of the resulting solution to 8. Then, the precipitated ZnO precursor powders (gel) were allowed to age for 12 h, followed by washing twice with deionized water. The dried powders were then ground in an agate mortar and subjected to thermal treatment in a muffle furnace at 500 °C for 4 h. Thus, ZnO nanosheets structures were obtained. The following steps were followed to obtain ZnO/GO nanosheets composite structures. Firstly, the mixtures obtained by dispersing 100 mg GO and 1 g ZnO nanosheets in 25 mL deionized water in two different beakers were subjected to ultrasonic treatment for 3 h to create a homogeneous distribution. As stated in the literature [33], the synthetization of GO/ZnO nanosheet composites relied on the principle of colloidal coagulation effect (CCE), which involved mixing equal volume ratios of GO solution and ZnO nanosheet solution mentioned above. After the mixture was obtained, it was continuously stirred at room temperature for 30 min, and then washed twice with ethanol before being dried at 50 °C for 12 h. Fig. 1 shows schematically synthesize procedure of the GO/ZnO nanosheet composites. Additionally, Sol-gel processes typically produce homogeneous products, ensuring consistency in important characteristics such as particle size, shape and distribution [34]. This uniformity is crucial for large-scale production and facilitates reproducibility in the final product. Numerical equations were obtained by using Python codes to optimize the synthesis process of ZnO nanosheets nanoparticles considering the experimental conditions determined in our study (see Fig. 2(b)). For this purpose, the precursor concentration (S) in molarity (M) as the independent variable and the average ZnO nanosheet size (B) obtained in nanometers (nm) as the dependent variable were considered. Since other external parameters such as temperature and pH were kept constant in the experimental process, only the precursor concentration was considered as the independent variable. Under these conditions, a regression model ($B = aS^b$) was established to describe the relationship between the precursor concentration and the average size of ZnO nanosheets. In this expression, B is the average particle size, S is the precursor concentration, "a" and "b" are the coefficients to be found as a result of regression. Regression model was performed using experimental data on the precursor concentration and the corresponding average crystallite size of ZnO nanosheets (SSP (black line), HW (red line) and WH (green line) approaches were used (see Fig. 2(b)) to obtain the "a" and "b" coefficients. The higher "a" value obtained even at low precursor Zn concentration, ZnO nanoparticles show significant basis sizes for ZnO nanoparticles even at low precursor concentrations, which requires precise optimization over the precursor concentration during production to avoid undesired nanoparticle growth. Also, Regression analysis of the three approaches used to determine crystallite size also showed positive 'b' values, indicating that the size of ZnO nanosheets increases with increasing precursor concentration. Therefore, the consistency of the 'a' and 'b' coefficients provides theoretical information for the adjustment of the Zn precursor concentration in order to obtain the desired particle sizes. In summary, our study has achieved systematic optimization of a number of variations under the specified experimental conditions for large-scale production through the regression model, with the aim of facilitating cost-effective production processes. In conclusion, the WH model to explain particle size shows that particle size varies with Zn precursor concentration with a variance of 94 % (adj. R^2 value) and additional factors (here distribution of reactant or precursor stoichiometry can be) affect particle size with a variance of 6 %.

In the study, the performance of ZnO nanosheets in the photocatalytic degradation of Simazine was investigated, with the aim of further enhancing the performance of the best-performing sample

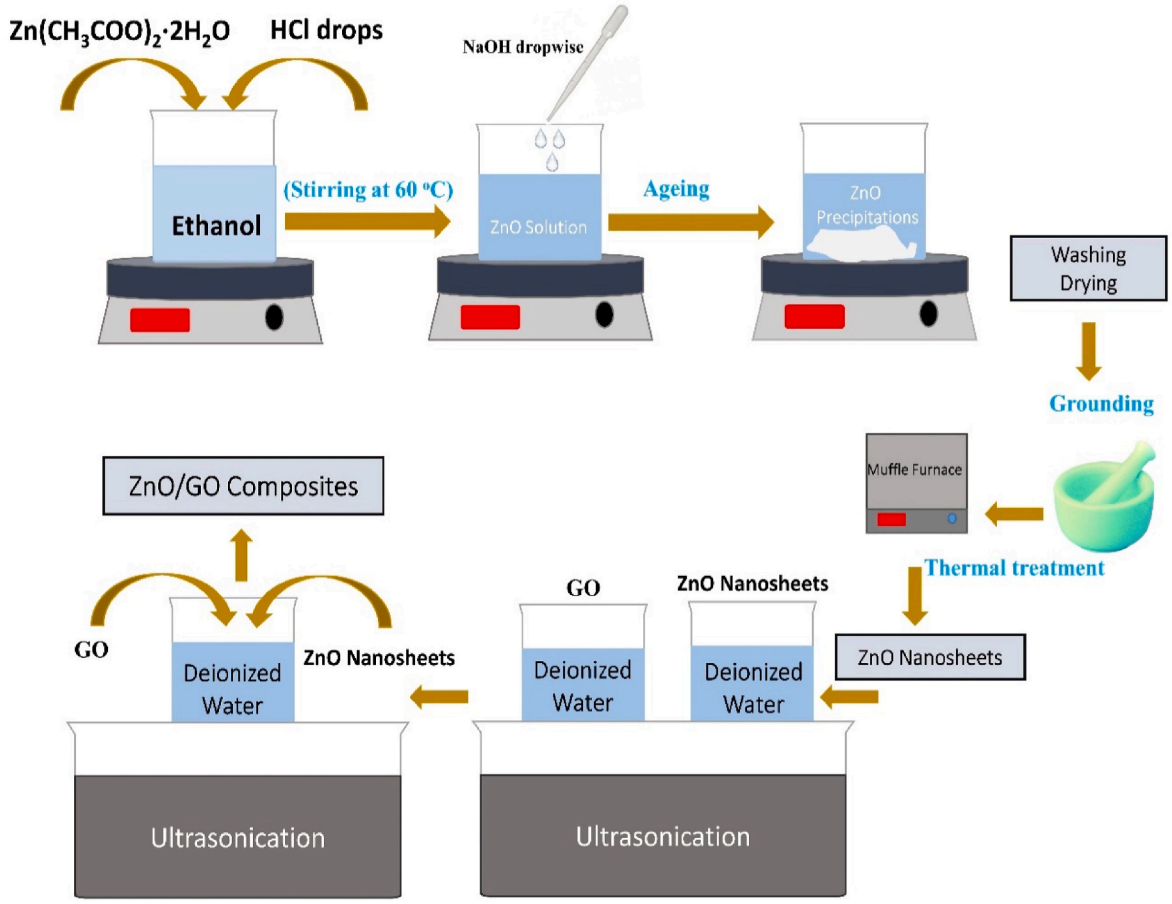

Fig. 1. Representation of experimental procedures for GO/ZnO composites.

through GO decoration. According to the obtained results, it was observed that the sample prepared with a concentration of 0.44 M zinc precursor salt exhibited the best performance with a degradation rate of 67 %. For that reason, this sample prepared with 0.44 M zinc precursor salt was decorated with GO, and thereafter, a nanocomposite denoted as ZnO/GO was synthesized. For photocatalytic research, experimental parameters were determined by taking into account the data in the study conducted by Flores et al. [35]. In the aforementioned study, the ZnO/GO nanocomposite exhibited high performance in the photocatalytic degradation of Simazine at a solution pH of 2 and a catalyst dosage of 40 mg. Therefore, similar experimental conditions were employed in our study. In photocatalysis experiments, a solution of Simazine prepared at a concentration of 1 ppm was kept in the dark for 30 min to ensure that the initial concentration of organic pollution remained constant at the beginning of the photocatalytic reaction for comparison. Photocatalysis studies on simazine were performed using a photo-reactor apparatus containing a Luzchem LZC-4X UVA lamp emitting light at a wavelength of 350 nm and a power density of 1000 W/m^2, with the UVA source placed 10 cm away from the simazine solution. The remaining simazine in solution was measured at certain times using a UV–vis spectrophotometer according to the Beer-Lambert law at 222 nm. This was used to evaluate the photocatalytic degradation performance. Furthermore, X-ray diffraction (XRD), scanning electron microscopy (SEM), thermogravimetric analysis (TGA), Fourier transform infrared spectroscopy (FTIR) and diffuse reflectance measurements were used to analyze the structural, morphological, thermal and optical properties of the synthesized samples.

3. Results and discussions

The thermal properties of the precursor have been the subject of investigation by means of TG-DTA measurements. For this purpose, at a temperature scan rate of 5°/min, the precursor was heated in a nitrogen atmosphere in an alumina crucible. Fig. 2(c) shows that the precursor lost weight in two stages. The initial weight loss (120–140 °C) is due to the removal of water molecules adsorbed on the surface, while the subsequent weight loss (140–400 °C) is attributed to the decomposition of $Zn(OH)_2$ into ZnO. This observation corresponds to the literature [36]. Supporting this observation, two endothermic peaks are clearly observed in the DTA curves, corresponding to the two weight loss steps in the TGA curve. In support of this observation, it has been clearly observed in DTA curves that correspond to the two weight losses in the TGA curve, manifesting two distinct endothermic peaks. The endothermic peak at approximately 130 °C, indicative of weight loss, observed on the surface of $Zn(OH)_2$ nanoparticles, as noted in the studies by Ref. [37], may be attributed to the dehydration of adsorbed water trapped on the surface. Additionally, the endothermic peak at 225 °C could be attributed to the loss of weight due to the release of OH^- ions. The cumulative weight loss of the precursor from room temperature to 400 °C is approximately 20 %, which closely aligns with the theoretical weight loss (18.48 %). This observation strongly suggests that the molecular formula of the precursor is $Zn(OH)_2$. Furthermore, the increasing trend in the DTA curve after 225 °C indicates the initiation of ZnO nucleation beyond this temperature point. XRD patterns of the synthesized ZnO nanosheet structures have been shown in Fig. 2 for various molarities. These results have been compared with the Joint Committee on Powder Diffraction Standards (JCPDS≠36–1451) X-ray data file, and the appearing peaks have exhibited good agreement with the hexagonal

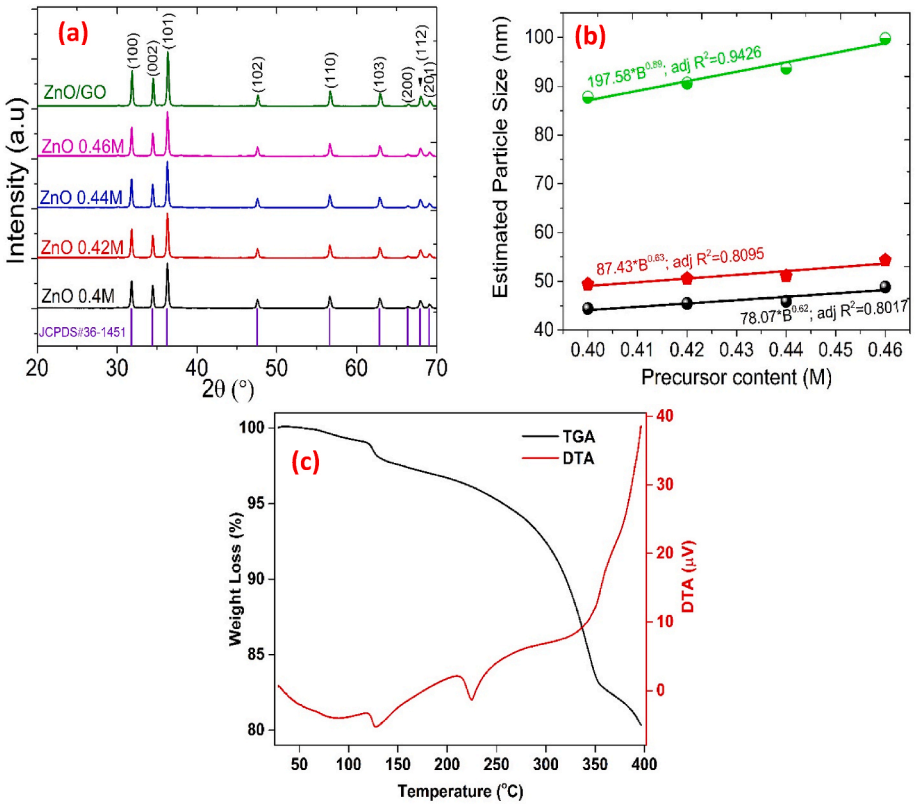

Fig. 2. XRD pattern of the samples (a) and regression model of predicting of the particle size (b), TGA/DTA analysis for precursor (c).

structure base. Furthermore, no characteristic diffraction peaks due to possible impurity phases such as C, $Zn(OH)_2$, etc. were observed, indicating the preparation of pure phase ZnO sample by sol-gel method. All samples were polycrystalline and exhibited the highest peak at around 36.28° (2θ) in the (101) plane. The thermal effect applied during the synthesis process is thought to be of critical importance in preferential orientation. At the same time, the observation of sharp peaks in the XRD diffraction patterns of the samples indicating high crystallinity strengthens this prediction.

Goswami et al. [38] mentioned in a study that high thermal energy can lead to re-crystallization in the ZnO lattice. Since trends or correlations between characteristics of the materials can provide information about the crystal structure, size and strain within the material, it is important to examine the correlation between these parameters for samples prepared for various molar concentrations of Zn precursor. In this context, parameters such as lattice parameters, interplanar distance, unit cell volume, bond length between Zn–O can be calculated using the following formulas [39,40];

$$a = \lambda \Big/ \sqrt{3} sin\,\theta \tag{1}$$

$$c = \lambda / sin\,\theta \tag{2}$$

$$\frac{1}{d^2_{(hkl)}} = \frac{4}{3\left[\frac{h^2+k^2+l^2}{a^2}\right]} + \frac{l^2}{c^2} \tag{3}$$

$$V = \frac{\sqrt{3}}{2} a^2 c \tag{4}$$

$$L = \sqrt{\frac{a^2}{3} + \left(\frac{1}{2} - u\right)^2} \tag{5}$$

The value "u" given in equation (5) is a positional parameter in the wurtzite hexagonal structure and indicates the amount of displacement of each atom relative to the next atom. Another word, the parameter "u" is used to describe the relative vertical displacement of the cation and anion layers along the c-axis. When "u" is equal to 0, it means that there is no displacement and the cation and anion layers are perfectly aligned. When "u" is not equal to 0, it indicates that the layers are displaced and it causes deviation from perfect alignment. The value of "u" can be easily calculated by the formula given in equation (6).

$$U = \frac{a^2}{3c^2} + 0.25 \tag{6}$$

The structural parameters of the samples prepared at different Zn precursor concentrations have been shown in Table 1. As can be seen here, Zn–O bond length increased until the zinc acetate concentration was 0.44 M, but decreased in the sample synthesized at 0.46 M concentration. Increasing the zinc acetate concentration (from 0.40 M to 0.44 M) means that we have more Zn ions available for incorporation into the crystal lattice of ZnO, which leads to an increase in Zn–O bond length. However, as observed in the sample synthesized at the more advanced zinc concentration (at 0.46 M zinc acetate concentration), there may be excess Zn ions, which can cause a decrease in these parameters by increasing Zn ions causing structural defects [41] such as interstitial atom and oxygen vacancies. Another reason for this may be the differences in ionic size between Zn–O ions [42]. Since "Zn" ions are larger than "O" ions, when you add more Zn ions to the crystal lattice, it disrupts the ideal packing of the smaller "O" ions. Considering that an ideal ZnO crystal should be arranged to accommodate larger Zn ions between smaller "O" ions, this size difference will create tension in the lattice [43]. The calculated sizes of the unit cell volume and the internal parameter values did not change appreciably as the concentration (molar) of the zinc precursor increased. Thus, it can be concluded that the geometry of the ZnO nanosheets does not change when the zinc concentration increases in agreement with the SEM photographs. Due to these observations, the amount of Zn precursor was increased up to 0.46

Table 1
Calculated structural parameters of the synthesized samples.

Sample	(hkl)	d $_{(hkl)}$ (Å)	FWHM (°)	V(Å)	u	L (nm)	Lattice Parameters	
							a (Å)	c (Å)
ZnO-0.40 M	(100)	2.8099	0.238	47.4869	0.3794	1.9729	3.2446	5.2086
	(002)	2.6001	0.203					
	(101)	2.4730	0.244					
	(102)	1.9092	0.277					
	(110)	1.6241	0.323					
	(103)	1.4759	0.348					
	(200)	1.4068	0.337					
	(112)	1.3780	0.348					
	(201)	1.3579	0.379					
ZnO-0.42 M	(100)	2.8097	0.234	47.4847	0.3793	1.9758	3.2444	5.2090
	(002)	2.6000	0.196					
	(101)	2.4729	0.243					
	(102)	1.9092	0.280					
	(110)	1.6240	0.323					
	(103)	1.4759	0.346					
	(200)	1.4068	0.321					
	(112)	1.3773	0.346					
	(201)	1.3578	0.383					
ZnO-0.44 M	(100)	2.8102	0.236	47.4956	0.3793	1.9759	3.2449	5.2086
	(002)	2.6004	0.199					
	(101)	2.4732	0.238					
	(102)	1.9093	0.280					
	(110)	1.6241	0.322					
	(103)	1.4768	0.343					
	(200)	1.4069	0.323					
	(112)	1.3780	0.345					
	(201)	1.3579	0.383					
ZnO-0.46 M	(100)	2.8096	0.225	47.4761	0.3793	1.9757	3.2442	5.2087
	(002)	2.5998	0.197					
	(101)	2.4728	0.235					
	(102)	1.9091	0.275					
	(110)	1.6240	0.317					
	(103)	1.4759	0.340					
	(200)	1.4061	0.333					
	(112)	1.3780	0.345					
	(201)	1.3578	0.370					

M, and this value was determined as the limit value of our study. Moreover, the characteristic diffraction peak of GO was not observed in the XRD pattern of ZnO-GO. This result is in agreement with some of literature [44,45], and the probable reason for this is the limited amount of GO that can change the structure of ZnO crystals. In summary, there are boundaries between crystal grains in ZnO and ZnO-GO nanocomposites. These boundaries are indicated by the presence of amorphous (non-crystalline) layers on the surface and between the grains of photocatalysts. These layers cannot be seen in X-ray diffraction (XRD) patterns commonly used to analyze the crystalline structure of materials. Considering the experimental conditions, it is considered as a very satisfactory explanation. The diffraction data also allow the calculation of the crystallite size (D) and intrinsic micro strain (ε) values of the materials. Within the scope of the study, these values were calculated and compared in terms of consistency by considering both the Williamson-Hall (WH), the Size-Strength plot (SSP) and the Halder-Wagner approaches (HW).

A more comprehensive understanding of the crystalline properties of materials can be achieved by analyzing crystallite size. Each method used for this purpose has its positive aspects and limitations. By using more than one approach, the results can be checked, and an idea about the reliability of the crystallite size values obtained can be obtained. The peak broadening caused by the strain induced by crystal defects and distortion is related to $\varepsilon \approx \beta/\tan\theta$ as stated by Ref. [46]. Furthermore, the dependence of Eq. (7) on the diffraction angle θ is important. The Williamson-Hall (W–H) method differs from the $1/\cos\theta$ dependence seen in the Scherrer equation [47,48], instead showing a relationship with the tangent of the Bragg angle ($\tan\theta$). This allows for a more nuanced analysis of X-ray diffraction peak broadening, as the W–H method can distinguish between reflection broadening caused by reduced crystallite size and microstrain occurring simultaneously. Therefore, the expansion reaches its peak due to the size and strain components. The total expansion can be formulated as follows:

$$\beta_{(hkl)} = \beta_{size} + \beta_{strain} \tag{7}$$

where, considering that β_{hkl} is the FWHM value for peaks at different diffraction planes, and β_{strain} is equal to $4\varepsilon\tan\theta$, expression (7) can be rewritten as follows:

$$\beta_{(hkl)} = \frac{1}{\cos\theta}\left[\frac{k\lambda}{D} + 4\varepsilon \sin\theta\right] \tag{8}$$

This equation is a kind of Williamson-Hall equation obtained as a result of uniform deformation modelling. Thus, a graph is drawn assuming an isotropic crystal structure where all material properties are direction-independent [49]. This means that the strain is the same in all crystallographic directions. The ($\beta\cos\theta$) vs. (4 $\sin\theta$) plot is drawn considering the preferential orientation peaks of the ZnO nanoparticles confirmed to have hexagonal wurtzite crystal phase using Eq. (8) and shown in Fig. 3.

The slope and *y*-intercept of the line fitted to the obtained pattern allow to analyze the strain and particle size, respectively. Based on the observation of Fig. 3, it can be concluded that all samples have a positive slope, and results belongs to uniform deformation model have been given in Table 2. It can be inferred that larger crystallites result in narrower diffraction peaks, leading to a positive slope in the W–H plot.

The W–H approximation has a non-zero slope and intercept, i.e. negligible (or) randomly distributed data points, indicating that all crystallites are isotropic with microstrain [50]. Furthermore, a common cause of peak broadening is size and strain within the crystal structure.

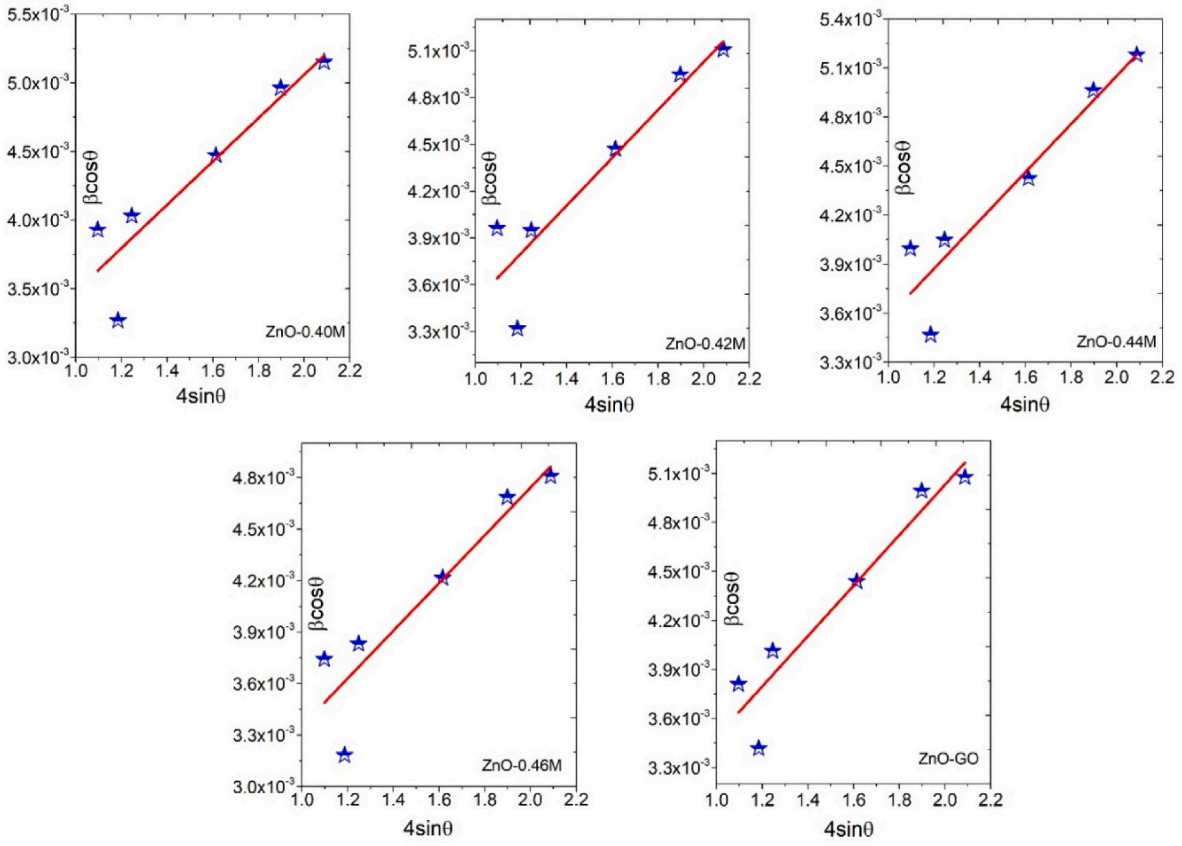

Fig. 3. Williamson–Hall plot for ZnO nanosheets.

Table 2
Comparison of crystallite sizes and micro strains calculated using WH, SSP and HW approaches.

Sample	SSP approach			HW approach			WH approach		
	D (nm)	$\varepsilon\times10^{-3}$	R^2	D (nm)	$\varepsilon\times10^{-3}$	R^2	D (nm)	$\varepsilon\times10^{-3}$	R^2
ZnO-0.40 M	44.44	9.12	0.91174	49.38	5.92	0.91174	87.75	1.90	0.84818
ZnO-0.42 M	45.46	9.20	0.89877	50.55	5.97	0.89870	90.62	1.96	0.85700
ZnO-0.44 M	45.91	9.37	0.88499	51.07	6.08	0.88498	93.68	2.10	0.88349
ZnO-0.46 M	48.82	10.01	0.92431	54.31	6.50	0.92431	99.75	1.96	0.85439
ZnO-GO	45.46	8.55	0.91202	50.22	5.31	0.90589	90.03	1.94	0.90908

Therefore, instead of evaluating the contribution of size and strain to peak broadening separately, direct information about the crystallite size and strain of the material can be obtained by considering the mean SSP [51]. In this approach, it is assumed that the mathematical functions describing the distribution of dimensions and strains within the material are characterized by Lorentzian and Gaussian profiles, respectively. For this purpose, Eq. (9) is obtained by modifying eq. (7) [52].

$$(d_{hkl}+\beta_{hkl}\,cos\,\theta)^2=\frac{0.9}{D}\left(d_{hkl}^2+\beta_{hkl}\,cos\,\theta\right)+\left(\frac{\varepsilon}{2}\right)^2 \tag{9}$$

In Fig. 4, $(d_{hkl}\beta_{hkl}\cos\theta)^2$ vs. $(d^2_{hkl}\beta_{hkl}\cos\theta)$ has been plotted considering the peaks indicated in the characteristic XRD diffractogram of ZnO nanoparticles with wurtzite hexagonal phase. The slope and the root of the *y*-intercept of the obtained graph indicate the crystallite size and strain, respectively. When the obtained results are compared with those obtained from the W–H approach, it can be concluded that there is a similar trend in crystallite size and strain depending on molarity and GO integration. The SSP method traditionally models the broadening of XRD peak profiles by assuming a Lorentzian function for the size contribution and a Gaussian function for the strain contribution. However, the actual XRD peak shape does not perfectly fit either a Lorentzian or Gaussian function [53].

The XRD spectrum's peak regions align well with the Gaussian function and effectively capture the central part of the profile. However, the tail part of the peak profile shows a rapid decay that cannot be accurately represented by a pure Gaussian function. This region shows a good agreement with the Lorentzian function. However, this model also fails to accurately represent the XRD peak region. Factors such as crystallite size, strain, defects and instrumental characteristics affect the complexity of the XRD peak profile, leading to the observed discrepancy [54,55]. To better understand the intricate details of XRD peak shapes, researchers should utilize more detailed approaches, such as hybrid functions or pseudo-Voigt function [56], to examine the consistency of the results. In this method, Eq. (10) can be written for determining FWHM.

$$\beta^2_{hkl}=\beta_L\beta_{hkl}+\beta^2_G \tag{10}$$

In eq. (10) β_L and β_G represent Lorentzian and Gaussian broadening of the XRD peaks. The important step required for the calculation of crystallite and strain with this approach is the calculation of the lattice distance (d_{hkl}) between the (*hkl*) planes. For hexagonal crystal structure, d_{hkl} can be related with the lattice constant as follow [57]:

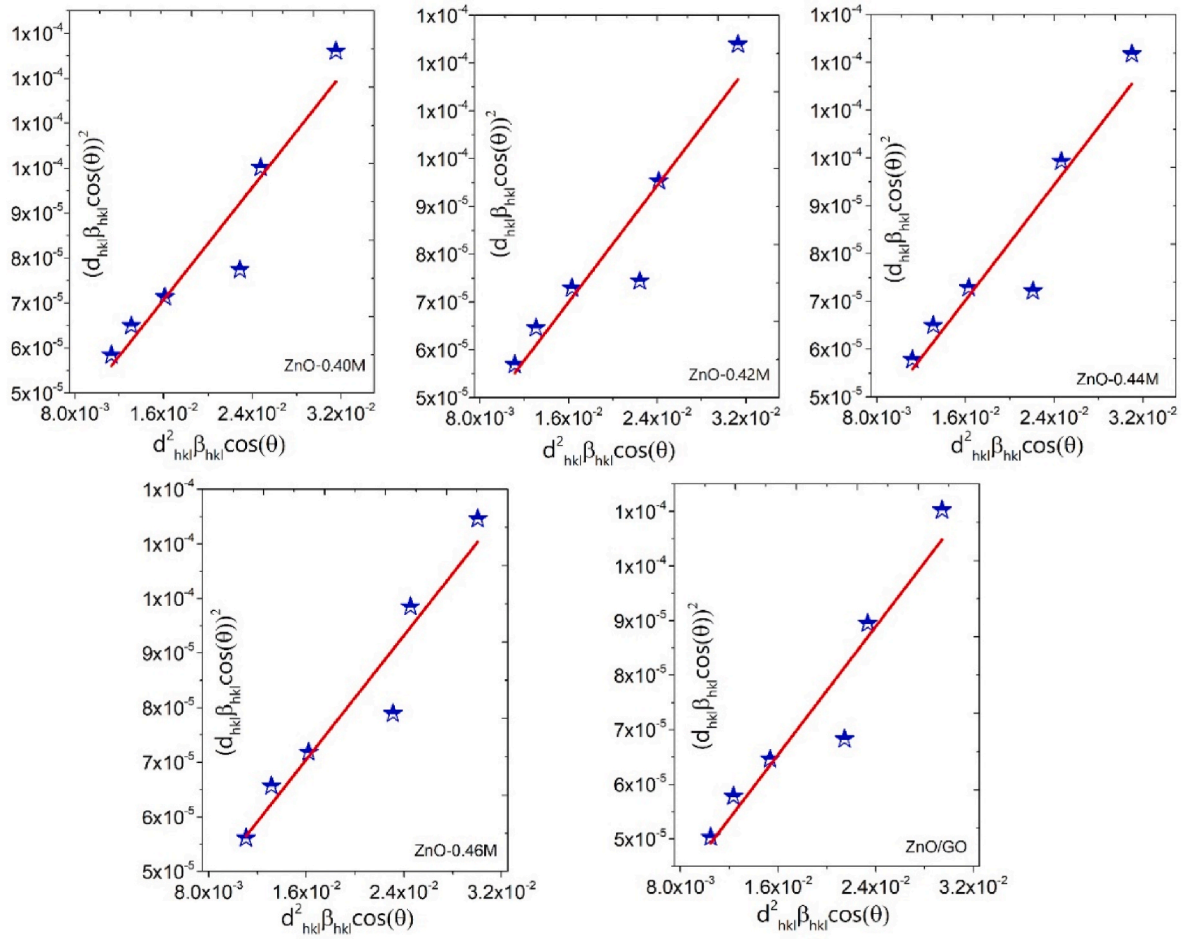

Fig. 4. The size-strain plot (SSP) plot for samples.

$$d_{hkl}^2 = \left(\frac{4\left(h^2+k^2+hk\right)}{3a^2} + \frac{l^2}{c^2}\right)^{-1} \tag{11}$$

Moreover, this method focuses on peaks at low and medium angles where the overlap of diffraction peaks is less, other formula to be used for the Halder-Wagner method can be categorized as in Eqs. (12)–(14) [58].

$$\left(\frac{\beta_{hkl}^*}{d_{hkl}^*}\right)^2 = \frac{1}{D}\frac{\beta_{hkl}^*}{{d_{hkl}^*}^2} + \left(\frac{\varepsilon}{2}\right)^2 \tag{12}$$

$$\beta_{hkl}^* = \beta_{hkl}\cos\theta/\lambda \tag{13}$$

$$d_{hkl}^* = 2\sin\theta/\lambda \tag{14}$$

The graph of $\beta_{hkl}^*/{d_{hkl}^*}^2$ vs. $\left(\frac{\beta_{hkl}^*}{d_{hkl}^*}\right)^2$ is obtained using Eqs. 10–14. The resulting graph is shown in Fig. 5. The crystallite size is determined by considering the mathematical inverse of the slope of the data fitted linearly to the graph in Fig. 5, while the root of the *y*-intercept gives the microstrain [59]. The results obtained by applying three different approaches to XRD data are given in Table 2. It is concluded that external effects such as molarity increase and GO hybridization in all three approaches meet the change in ZnO crystal structure with a similar trend. This trend shows that the average crystallite size increases with increasing concentration of zinc precursor salt. High zinc concentrations increased the formation of agglomerates during the precipitation process, which is the most likely reason for this situation. Similar observations have been made by other researchers who synthesized nanoparticles using the solution-based method [60,61]. Furthermore, the average particle size of the ZnO/GO nanocomposite structure was reduced compared to that of the pure ZnO structure. The possible reason for this could be the division of larger nanoparticles during the synthesis of the ZnO/GO composite through the colloidal coagulation effect. Morphological analyses of the synthesized samples have been evaluated by SEM analysis. Fig. 6 reveals SEM images of the ZnO that most of the ZnO nanoparticles are in the geometry of nanosheets, and their size increase with increasing zinc concentration, as revealed by the histogram curves embedded in the SEM photographs. The results are larger than compared to the values calculated from XRD and are in agreement with the trend resulting from the effect of zinc salt concentration and GO. This can be explained in relation to the geometries of the obtained ZnO nanosheets. Namely, the nanosheets agglomerated in a way that can be attributed to the large specific surface area and high surface energy, which is presumed to have occurred during the post-sintering cooling process [62]. The formation of ZnO nanocrystals requires directional growth, followed by differential aggregation in the respective media, and subsequent formation of nanosheet structures through nucleation. This process occurs when the concentration of precursors (i.e. nanocrystals or monomers) exceed the critical supersaturation level [63]. To better understanding about the nucleation process, it should consider the chemical reactions. Formations of ZnO nanosheets in alcoholic medium can be summarized as follow:

$$Zn(CH_3COO)_2 \bullet 6H_2O + 2HCl \rightarrow ZnCl_2 + 2CH_3COOH + 6H_2O \tag{15}$$

$$Zn^{2+} + 2OH^- \rightarrow Zn(OH)_2 \tag{16}$$

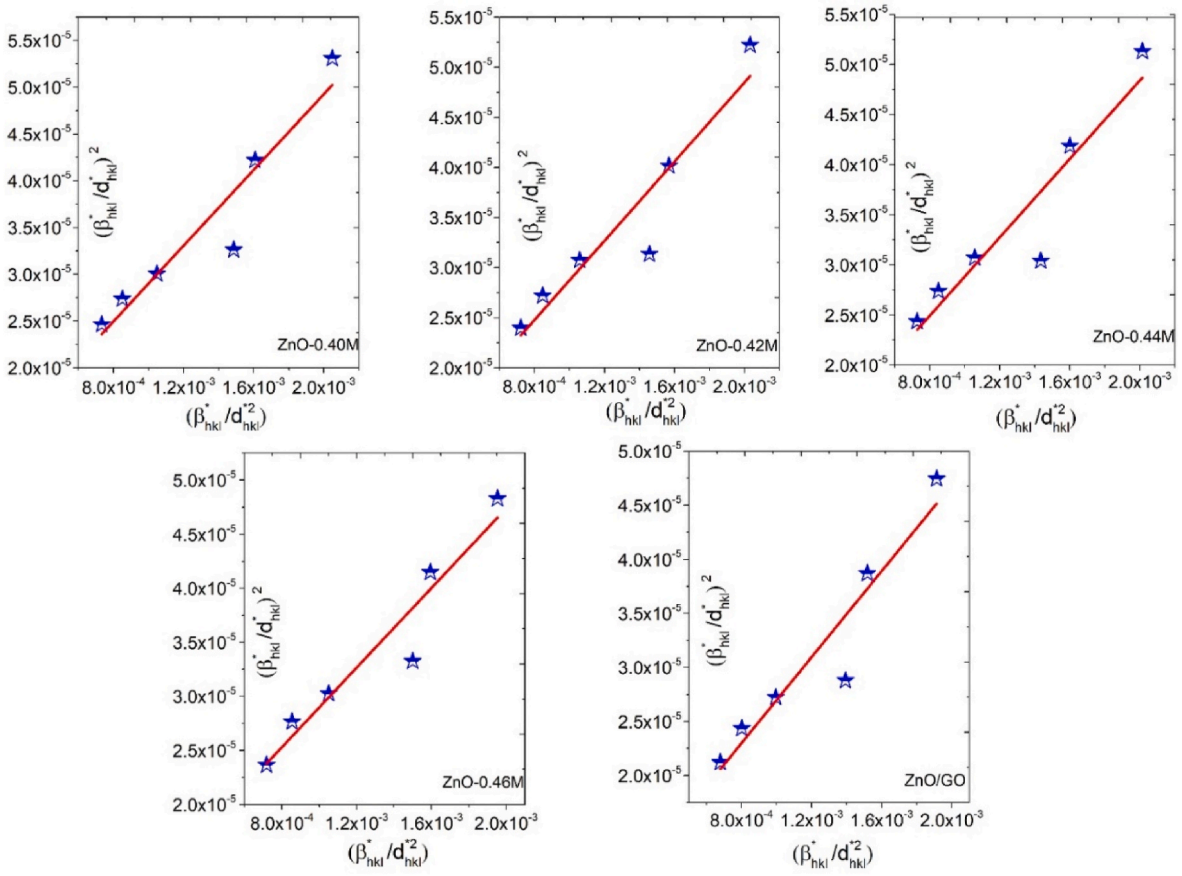

Fig. 5. Halder-Wagner plot for ZnO nanoparticles.

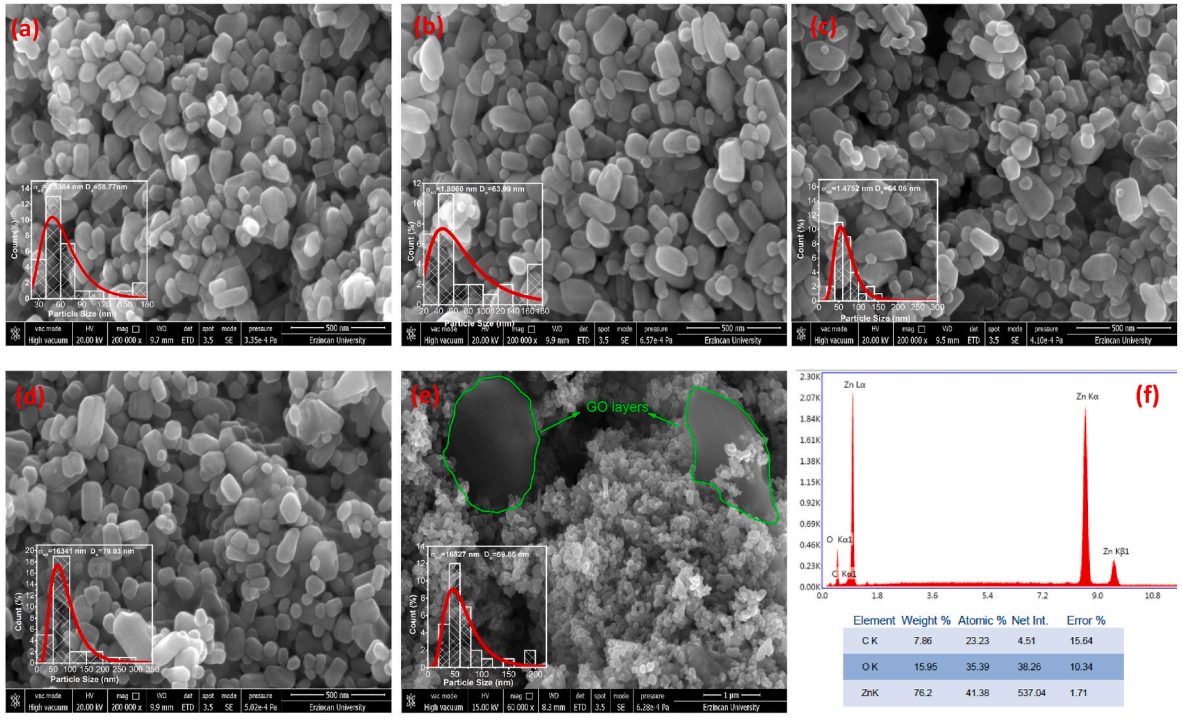

Element	Weight %	Atomic %	Net Int.	Error %
C K	7.86	23.23	4.51	15.64
O K	15.95	35.39	38.26	10.34
ZnK	76.2	41.38	537.04	1.71

Fig. 6. SEM images of ZnO nanosheets and ZnO/GO composite a) 0.40 M b) 0.42 M c) 0.44 M d) 0.46 M e) ZnO/GO and f) EDX spectra of ZnO/GO nanocomposite.

$$Zn(OH)_2 \rightarrow ZnO + H_2O \quad (17)$$

$$ZnO\ assembly\ into\ nanosheets\ during\ the\ calcination \longrightarrow ZnO_{nanosheets} \quad (18)$$

In the initiation reaction step, Zn^{2+} from $ZnAc_2$ used as zinc precursor and OH^- ions from ethanol coordinate with each other to form aggregates of the type $(Zn_XOH_y)^{2x-y}$ exhibiting octahedral coordination sequences [64]. Depending on the used medium (in this case ethanol), the initially randomly oriented nanocrystals begin to aggregate with different tendencies. After the nanocrystals aggregated, the nanosheets may have formed by random Brownian motion collisions [65], interparticle fusion [63,66], or interparticle molecular exchange (dissolution and diffusion), also known as Ostwald ripening and defect density difference [67]. Fig. 6(e) clearly shows the wrinkled GO sheets and ZnO nanosheets coated on the GO sheets. It is suggested that there is a strong interaction between ZnO particles and GO layers. This strong interaction prevents the exfoliation of GO layers during photocatalysis applications and ensures efficient processes [68]. Indeed, our photocatalysis results confirmed this prediction. In addition, the particle size reduction observed in the XRD results and estimated as the cleavage of existing ZnO nanoparticles during hybridization with GO is also clearly seen in the SEM photographs. Fig. 6(f) presents the EDX results, confirming the elemental composition. The weight percentages obtained are acceptable, considering the incorporation of graphene oxide into the ZnO nanoparticles. The carbon and oxygen percentages are consistent with the presence of graphene oxide, while the predominant zinc percentage is consistent with the ZnO component. The structural analysis of the synthesized compounds can be strongly investigated by FTIR spectroscopy. FTIR spectroscopy of ZnO nanosheets and ZnO/GO nanocomposite particles are shown in Fig. 7. It has been shown by XRD analysis that high quality crystals were obtained with increasing zinc precursor salt concentration. In support of this observation, sharp peaks were observed in the FTIR spectrum. Furthermore, samples prepared at increasing zinc concentration up to 0.46 M exhibited high transmittance. Taking into account dislocations, which are a kind of defects in a crystalline material, and their density ($\delta = {}^{1}/_{D^2}; D$: *estimated crystallite size*) [69], changes in the local environment of Zn–O bonds due to the reduction of defects may have reduced absorption and thus achieved high transmittance.

On the other hand, there was a decrease in optical transmittance in the sample prepared at 0.46 M precursor zinc salt concentration. Moreover, there was a decrease in optical transmittance in the sample prepared at 0.46 M precursor zinc salt concentration. The observation of a similar trend in the Zn–O bond length strengthens the idea that this concentration value indicates a saturation or equilibrium point. In other words, it can be predicted that the structural and chemical properties of the material to be obtained after a certain concentration will not change significantly. This is thought to lead to the stabilization of the FTIR spectrum. The transmittance band observed at about 697 cm^{-1} in Fig. 7 (given as "A" in the figure) can be attributed to Zn–O stretching, indicating that ZnO nanosheets are positively obtained [70]. The peak indicated by B (at 879.65 cm^{-1}) in Fig. 7 can potentially be attributed to specific vibrations within the zinc-hydroxy-acetate complex, given that zinc acetate-based synthesis was performed [71]. The C═O vibration band, which is also contributed by acetate ions ($Zn(CH_3COO)_2$), which is a source of zinc, is dominant at 1427.57 cm^{-1} (C point in Fig. 7) as Thongam et al. [72]. Moreover, the broad absorption band observed at about 3000 cm^{-1} in the ZnO/GO nanocomposite is attributed to the stretching vibration of the surface hydroxyl groups (-OH) [73].

As stated in the literature, ZnO crystallizes in the hexagonal wurtzite structure, which belongs to the C46v space group [74]. According to group theory there can be eight sets of phonon modes, 2E2, 2A1, 2E1 and 2B1, but 2B1 is not Raman-active. When the incident and scattered polarizations are perpendicular, only the E2 mode is observed in Raman measurements (see Fig. 7 (b)). In this context, the high frequency E2 mode is clearly visible at 426 cm^{-1}. According to the literature [75], certain modes may not be detectable in the Raman spectrum due to variations in crystallite size. In our study, we investigated the effect of varying the concentration of the Zn precursor salt on the size of ZnO nanoparticles' crystallites. As a result, there was agglomeration, which changed the electronic environment of the nanoparticles, which can lead to the appearance of fluorescent regions that block the E2 mode. This explanation has been mentioned as a possible reason for the

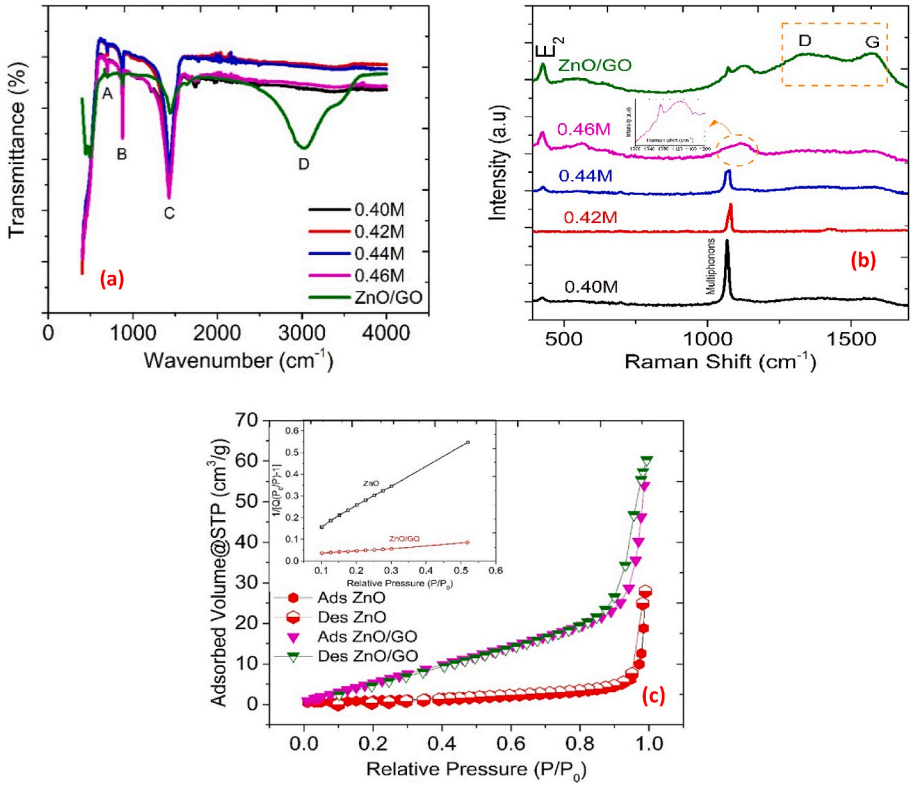

Fig. 7. FTIR (a) and Raman (b) spectra and BET analysis (c) of the samples.

non-observation the E2 mode in some examples. Furthermore, multiple A1-symmetric phonons were observed at around 1075 cm^{-1}, indicating that multiple phonons absorbed or emitted simultaneously during the scattering event [76]. In addition, in the Raman spectrum obtained for ZnO/GO composite material, peaks belonging to D (observed at 1336 cm^{-1}) and G (observed at 1577 cm^{-1}) bands typical for GO were clearly observed. This result is fully consistent with the literature [77]. The Raman spectrum of the ZnO/GO sample shows a decrease in the intensity of the ZnO Raman peak, suggesting a weaker intensity. Also, Fig. 7(b) illustrates that the intensity of the D band is slightly higher than that of the G band. This suggests that high defect regions in the graphene lattice, as indicated by the D/G ratio, serve as useful nucleation sites for ZnO [78]. As a result, there is less agglomeration of ZnO nanoparticles, which is consistent with the photocatalytic performance of the ZnO/GO sample. Photocatalytic processes are influenced significantly by the active reaction area on the catalyst's surface. In order to determine the physical properties such as surface area and porosity of the ZnO prepared at a precursor concentration of 0.44 M Zn and the ZnO/GO nanocomposite, a Brunauer-Emmett-Teller (BET) surface area analysis was carried out. For this purpose, under the N_2 adsorption/desorption isotherm at ~77 K, the BET surface areas of the samples were reordered. Isotherm and multi-point fit curves of the samples are shown in Fig. 7(c). The samples reflected the isotherm of type IV, showing a curve that rises slightly as the volume of gas adsorbed increases and then rises at a slow rate [79]. This indicates that there are pores and voids in the material. The multipoint graph indicates that the surface area of ZnO and ZnO/rGO samples are 3.9860 and 24.5961 m^2/g, respectively. Additionally, compared to the ZnO/GO sample, the BET measurement shows that the surface area of ZnO is significantly lower. Moreover, the cumulative pore volumes and sizes of ZnO and ZnO/GO samples were found to be 0.0100, 0.0487 cm^3/g and 31.70,11.37 nm, respectively. These obtained results from BET analysis are consistent with the performance of ZnO/GO sample in the photocatalytic degradation of simazine.

In order to get information about the optical properties of the synthesized nanoparticles and ZnO/GO composite, the UV–Vis diffuse reflectance spectra (DRS) of the samples were analyzed and Kubelka-Munk function vs. energy curves have been presented in Fig. 8. The change in the band gap with increasing concentration of $Zn(Ac)_2$–$6H_2O$ was analyzed by fitting the absorption characteristics obtained from diffuse reflectance data to the $(\alpha h\nu) = A(h\nu - Eg)^{0.5}$ expression (Fig. 8) [80,81]. According to Fig. 8, it has seen that the optical band gap values increased with the increasing $ZnAc_2 \bullet 6H_2O$ content. The increase in the band gap is attributed to the increase in particle size, which is a consequence of the increasing concentration of $Zn(Ac)_2 \bullet 6H_2O$, as observed in Ref. [82]. One possible explanation for the lower band gap observed in small particle nanoparticles is the increased band bending at the grain boundaries. This is a result of the higher grain surface area of samples with a smaller grain size [83]. Fig. 8(e) shows that the band gap of ZnO/GO decreases to 2.94 eV after GO is added to ZnO. In many studies examining the effects of ZnO/GO composite in the literature, a decrease in the band gap of zinc oxide was encountered after the addition of GO. The authors explain this observation by relating it to chemical bonds such as Zn–O–C or Zn–C bonds formed in the composites. Alamdari et al. [84], mentioned that this reduction may be the result of the absorption of part of the light by the heterogeneous bands of Zn–O–C and also by the carbon structure in the sample. Also, Puneetha et al. [85] mentioned in their study that the narrowing of the band gap

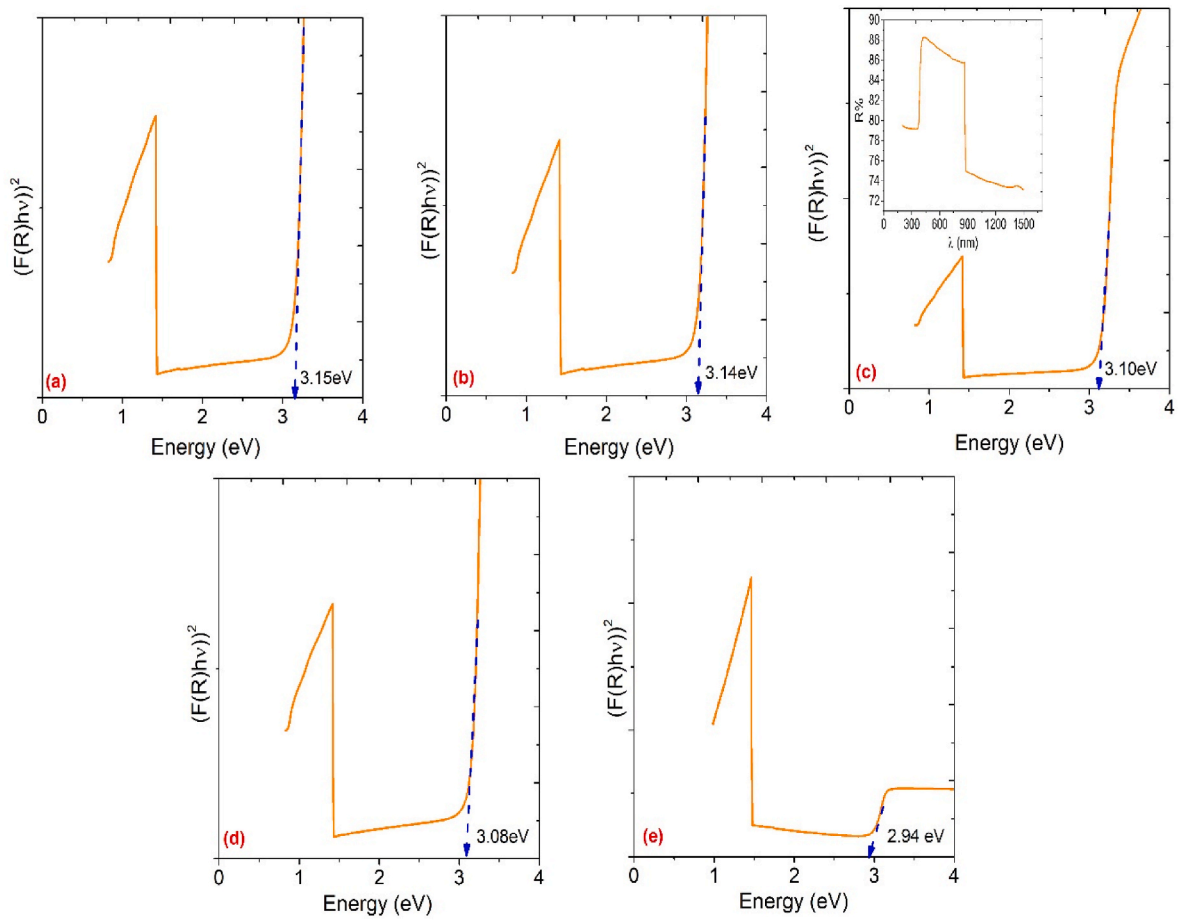

Fig. 8. Plots of the Kubelka-Munk function vs. energy for the determination of the band gap for zinc oxide nanostructures synthesized at different concentrations. a) 0.46 M b) 0.44 M c) 0.42 M d) 0.40 M e) ZnO/GO.

due to the presence of GO is a result of the increased surface charge between the ZnO nanoparticle and the GO layer, and thus increased electronic coupling. That is, the presence of GO clears the ZnO conduction band by transporting excited electrons to the GO layer via π electrons and quenches the Burstein-Moss effect. As a result, the Fermi energy level decreases, narrowing the band gap and approaching valence band. In addition, Durmus et al. [86], reported that the decrease in the optical bandgap with GO doping in a similar composite material. They said that the size reduction of ZnO particles during the synthesis of the composite structure may be due to the 2D order and the limited agglomerated structure on the GO nanosheet. In addition, the bandgap energy of ZnO was observed to remain unchanged despite the presence of two different phases (ZnO nanoflakes and GO) in the ZnO/GO nanocomposite heterojunction as reported in the literature [87]. This is likely attributed to the experimental method used in the synthesis of the nanocomposites.

Fig. 9 shows the photocatalytic degradation of herbicide Simazine after 180 min of UVA exposure, using ZnO nanosheets and ZnO/GO composite powders as catalysts. In photocatalytic investigations, UVA light was used as irradiation source, while simazine was used as organic pollutant. UVA light was used as the light source in this study because UVA light is very similar to natural sunlight, which contains a significant portion of UVA radiation, can penetrate photocatalytic materials more deeply than short wavelengths such as UVB and UVC, and most photocatalytic materials exhibit optimum photocatalytic activity under UVA light [97]. As shown in Fig. 9(a–e), the absorption intensity of the illuminated solutions decreased in the presence of ZnO nanosheets, and this decrease was maximized in the presence of ZnO/GO. In general, this decrease can be attributed to the fact that ZnO nanosheets absorb UVA light to form electron (e^-) hole (h^+) pairs that can directly or indirectly degrade simazine (such as hydroxyl radicals) [98]. In the experiment where ZnO nanosheets prepared with 0.40 M–0.46 M zinc precursor salt were used as catalyst, the sample prepared with 0.44 M zinc precursor salt provided a maximum degradation of 67 % at the end of 180 min UVA irradiation as shown in Fig. 9(f–g). However, when the samples prepared with 0.46 M zinc precursor salt were considered, this ratio decreased to 47 %. Mass transfer and diffusion of reactants and products in photocatalytic processes is a very important parameter. Considering XRD and SEM analyses, increasing precursor concentration led to higher crystallite size. It is estimated that this may be due to the limitation of access to active sites as a result of increased agglomeration of nanoparticles prepared at 0.46 M precursor concentration, thus preventing the degradation of simazine molecules. In addition, the optical characteristics of the sample prepared at a precursor concentration of 0.46 M (see Fig. 8(a)), which affects the formation and separation of electron-hole pairs under UVA irradiation, may also be responsible for this.

Therefore, the nanosheets with the highest performance in the photocatalytic degradation of Simazine under UVA light (here, nanosheets prepared at a zinc precursor salt concentration of 0.44 M) were further enhanced by incorporating graphene oxide (GO) into the composite structure. As expected, with the addition of GO, Simazine was photocatalytically degraded by 85 % (see Fig. 9(f–g)). In the literature, some researchers have studied the reaction mechanisms of simazine degradation in UV/TiO_2 system in a broad perspective [3,89]. This study also has shown same type reactions. Reaction mechanisms for the UV/ZnO-GO system can be written as shown in Eqs. (19)–(22):

$$ZnO + h\nu \rightarrow e_{cb}^- + h_{vb}^+ \rightarrow GO + e_{cb}^- \rightarrow GO\left(e_{cb}^-\right) \quad (19)$$

$$GO\left(e_{cb}^-\right) + O_2 \rightarrow \bullet O_2^- + H_2O \rightarrow \bullet OH \quad (20)$$

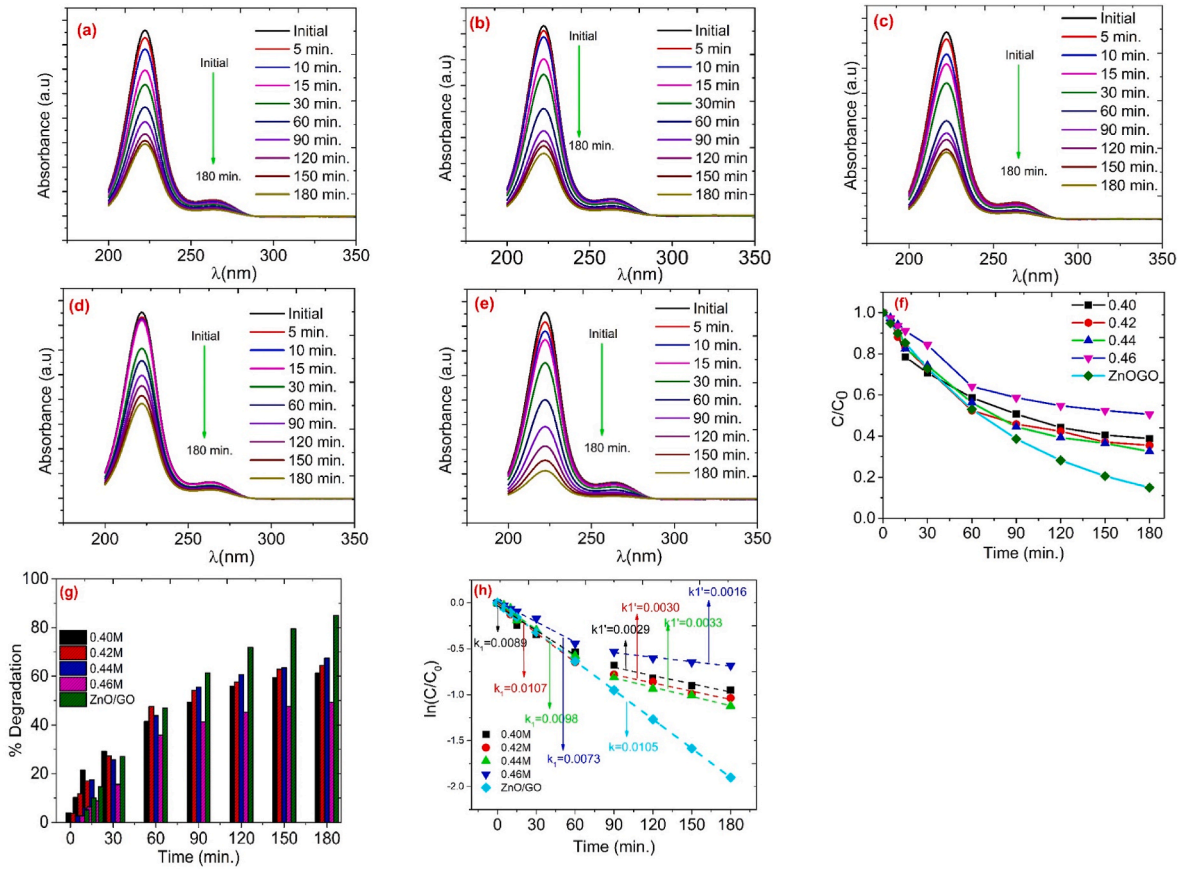

Fig. 9. Photoreduction of Simazine (ZnO catalyst obtained at 0.40 M (a), 0.42 M (b), 0.44 M (c), 0.46 M (d), and ZnO/GO (e)), C/C_0 curves (f), % degradation vs. time plot of Simazine (g) and kinetic ($\ln(C/C_0)$) vs time curves (h) of simazine in photocatalytic degradation.

$$h_{vb}^{+} + H_2O \rightarrow \bullet OH + H^{+} \quad (21)$$

$$\bullet OH + Simazine \rightarrow Intermediates \rightarrow CO_2 + H_2O \quad (22)$$

According to the mentioned equations, when the ZnO/GO nanocomposite is exposed to UV light, energy transfer to electrons occurs due to the effect of irradiation, and the electrons jump from the valence band to the conduction band of ZnO, leaving holes behind. After this step, the electrons that move from the conduction band of ZnO to GO combine with oxygen molecules to form superoxide species, which in turn interact with water molecules to produce hydroxyl radicals. Simazine mainly contains nitrogen atoms in the triazine ring structure, but carbon atoms are also present in the aromatic rings attached to the nitrogen atoms, allowing hydroxyl radicals ($\bullet OH$), superoxide radicals ($\bullet O_2^-$) and holes (h^+) to attack the simazine molecule at various carbon atoms through oxidation reactions to form intermediates corresponding to different m/z. As can be seen from Fig. 9(f–g), the degradation efficiency of simazine has significantly enhanced by the interaction of ZnO with GO. In this way, the ability of the photocatalyst to degrade persistent organic pollutant has been achieved. Moreover, considering the performance of the studied nanocomposite of ZnO/GO, it can be thought as a preferable catalyst for organic pollutants for the herbicide group in Table 3. The synergistic effect created by the presence of graphene oxide in close proximity to ZnO makes them electron acceptors and carriers for efficient separation of the photo-charge carrier from bare nanostructures, creating additional surfaces where electrons and holes can be spatially separated. This ensures efficient charge separation by reducing the probability of electron-hole encounters [99]. In addition, due to the high electron affinity of graphene oxide (GO) compared to ZnO, the energy level between the conduction band of ZnO and the π* orbitals of GO is aligned (Eq. (19)) and photogenerated electrons are transferred to GO, preventing electrons from recombining with holes in the valence band of ZnO [100]. Besides, the decrease in the optical bandgap of the ZnO/GO nanocomposite as a result of the synergistic effect between ZnO and GO is shown in Fig. 8(e). This means that the nanocomposite can absorb a wider range of light wavelengths, including visible light, and thus act as an efficient catalyst by obtaining a high density of photogenerated charge carriers. Numerous studies investigating the photocatalytic degradation of organic pollutants using ZnO as a catalyst have shown that the degradation rates obey Langmuir-Hinshelwood kinetics [101–104]. The expression showing that photocatalytic degradation occurs via Langmuir-Hinshelwood first order reaction [17] is shown in Eq. (23).

$$ln\frac{C}{C_0} = kt \quad (23)$$

Fig. 9(h) has been obtained using Eq. (23). The slope of this graph gives the rate constant (k) and the half-life time ($t_{1/2}$) can be obtained using Eq. (24).

$$t_{1/2} = ln\,2/k \quad (24)$$

The values of kinetic parameters are shown in Table 4. Accordingly, it is seen that the value of $t_{1/2}$, which is inversely proportional to the rate constant, decreases with increasing rate constant. Fig. 9(h) clearly shows that the rate of reaction slows down after 60 min. This can be explained by the concentration of organic impurities remaining in the solution after a certain time, as observed in the study by Yang et al. [105]. So, considering Fig. 9(f–g), 67 % of the maximum degradation can be mentioned. In this case, relatively high dye concentration is present in the reaction solution at the end of 60 min, so that mass transport limitations, which can be related to the rate at which dye molecules reach the catalyst surface, dominate the overall reaction kinetics.

In addition, a constant reaction rate was observed throughout the whole process with GO integration into ZnO. Graphene oxide (GO) is effective in adsorbing organic pollutants onto the composite surface due to its high surface area and abundance of functional groups. Therefore, this observed phenomenon can be explained by the presence of GO in the composite structure, which provides a continuous supply of reactant to the ZnO photocatalyst surface leading to a constant reaction rate. In addition, the R^2 values shown in Table 4 were found to be close to 1, indicating that the photocatalytic process strongly fits the first-order kinetic model.

4. Conclusion

In the scope of this research, ZnO nanosheets and ZnO/GO nanocomposite structures were synthesized via a facile and easily applicable sol-gel method. Structural characterization results confirmed that the obtained samples possess the characteristic hexagonal wurtzite crystal structure of ZnO, and the increased zinc precursor concentration influenced the size of the nanosheets. The structural characterization of the samples was conducted through FTIR analysis, revealing characteristic spectrum peaks corresponding to ZnO and ZnO/GO structures. Additionally, optical bandgaps of the samples were calculated based on diffuse reflectance results, showing an increase in the optical bandgap with the increasing concentration of zinc precursor salt. This observation was associated with the increased particle size due to the zinc precursor salt. The photocatalytic activity of the synthesized samples

Table 4
Kinetic parameters of Simazine degradation.

Catalyst	k_1 (min^{-1})	$k_1^{'}$ (min^{-1})	$t_{1/2}$ (min.)	$t_{1/2}^{'}$ (min)	R^2	R^2
ZnO-0.40 M	0.0089	0.0029	77.881	239.016	0.9443	0.9486
ZnO-0.42 M	0.0107	0.0030	64.780	231.049	0.9959	0.9690
ZnO-0.44 M	0.0098	0.0033	70.729	210.044	0.9831	0.9907
ZnO-0.46 M	0.0073	0.0016	94.951	433.216	0.9858	0.9758
ZnO/GO	0.0105	–	66.014	–	0.9998	–

Table 3
Comparison of the performances of the catalysts reported in the literature in the photocatalytic degradation of commonly used herbicides.

Catalyst	Light Source	Pollutant	%degradation	Time (min.)	Ref.
TiO_2 Nanotubes	UV	Simazine	57.4	240	[88]
TiO_2 Nanotubes	UV	Simazine	60	240	[89]
$Ni@NiFe_2O_4/TiO_2$ +PMS	Solar	Simazine	99	240	[90]
FTO-$BiMoVO_4$	Solar	Simazine	100	120	[2]
Au–TiO_2 (Sonophotocatalysis)	UV	Simazine	43	420	[91]
AFG@30MIL(Fe)	Visible	Atrazine	81	105	[92]
ZnO–TiO_2	UV	Atrazine	87	120	[93]
WO_3	UV	Diazinon	99	120	[94]
hydrogenated F-doped TiO_2	UV	Atrazine	87.58	180	[95]
Cu–ZnO/g-C_3N_4.	Visible	Atrazine	> 80	120	[96]
ZnO/GO	UVA	Simazine	85	180	This work

was studied under UVA illumination in the presence of Simazine. After 180 min of illumination, samples prepared with 0.40 M, 0.42 M, 0.44 M, and 0.46 M zinc precursor salts have degraded Simazine by 62 %, 64 %, 67 %, and 46 %, respectively. The sample exhibiting the highest performance was integrated with GO to obtain ZnO/GO nanocomposite, resulting in the degradation of 85 % of Simazine within the same duration. This indicates reduced recombination losses, proving effective charge separation. Additionally, the ZnO/GO nanocomposite exhibited a constant reaction rate (0.0105 min^{-1}) throughout the entire reaction and showed a high R^2 value close to 1, indicating strong agreement with the first-order kinetic model, further validating its photocatalytic performance.

CRediT authorship contribution statement

Sakir Aydogan: Formal analysis, Writing – original draft. **Nurtac Canpolat:** Investigation, Methodology, Writing – review & editing. **Adem Kocyigit:** Formal analysis, Investigation, Methodology, Writing – original draft. **Mehmet Yilmaz:** Conceptualization, Formal analysis, Investigation, Methodology, Software, Writing – original draft, Writing – review & editing.

Declaration of competing interest

The authors declare that they have no known competing financial interests or personal relationships that could have appeared to influence the work reported in this paper.

Acknowledgements

Authors would like to thank Bilge Eren, Gökhan Sevinç and Cagri Cirak for their assistance on the measurements.

References

[1] A. Aldeguer Esquerdo, P.J. Varo Galvañ, I. Sentana Gadea, D. Prats Rico, Activated carbon and ozone to reduce simazine in water, Water 12 (2020) 2900, https://doi.org/10.3390/w12102900.
[2] J. Xu, H. Olvera-Vargas, F.Y.H. Teo, O. Lefebvre, A comparison of visible-light photocatalysts for solar photoelectrocatalysis coupled to solar photoelectro-Fenton: application to the degradation of the pesticide simazine, Chemosphere 276 (2021) 130138, https://doi.org/10.1016/j.chemosphere.2021.130138.
[3] W. Chu, Y. Rao, W.Y. Hui, Removal of simazine in a UV/TiO 2 heterogeneous system, J. Agric. Food Chem. 57 (2009) 6944–6949, https://doi.org/10.1021/jf9012482.
[4] F. Grasselli, S. Bussolati, R. Ramoni, S. Grolli, G. Basini, Simazine, a triazine herbicide, disrupts swine granulosa cell functions, Anim. Reprod. 15 (2017) 3–11, https://doi.org/10.21451/1984-3143-2017-AR960.
[5] E.G. Søgaard, R. Aruna, J. Abraham-Peskir, C. Bender Koch, Conditions for biological precipitation of iron by Gallionella ferruginea in a slightly polluted ground water, Appl. Geochem. 16 (2001) 1129–1137, https://doi.org/10.1016/S0883-2927(01)00014-2.
[6] C. Zhao, G. Hao, H. Li, Y. Chen, Supercritical fluid extraction for the separation of organochlorine pesticides residue in Angelica sinensis, Biomed. Chromatogr. 16 (2002) 441–445, https://doi.org/10.1002/bmc.180.
[7] M. Andrunik, T. Bajda, Removal of pesticides from waters by adsorption: comparison between synthetic zeolites and mesoporous silica materials. A Review, Materials (Basel) 14 (2021) 3532, https://doi.org/10.3390/ma14133532.
[8] J.T. Alexander, F.I. Hai, T.M. Al-aboud, Chemical coagulation-based processes for trace organic contaminant removal: current state and future potential, J. Environ. Manag. 111 (2012) 195–207, https://doi.org/10.1016/j.jenvman.2012.07.023.
[9] I.A. Saleh, N. Zouari, M.A. Al-Ghouti, Removal of pesticides from water and wastewater: chemical, physical and biological treatment approaches, Environ. Technol. Innov. 19 (2020) 101026, https://doi.org/10.1016/j.eti.2020.101026.
[10] T. Sun, Z.-Y. Jin, B. Deng, G. He, Q.-Y. Wang, M. Hu, Z. Han, Z. Zheng, J. Zhao, J. Yun, J. Zhao, Y. Zhu, Z. Pan, X. Li, Z.-T. Hu, Visible-light-driven photo-Fenton oxidation enhanced by Fe/Bi-nanocrystal phase transformation as a universal way for various organic pollutants mineralization, Chem. Eng. J. 481 (2024) 148732, https://doi.org/10.1016/j.cej.2024.148732.
[11] M.P. Ormad, N. Miguel, A. Claver, J.M. Matesanz, J.L. Ovelleiro, Pesticides removal in the process of drinking water production, Chemosphere 71 (2008) 97–106, https://doi.org/10.1016/j.chemosphere.2007.10.006.
[12] M. Kanwal, S.R. Tariq, G.A. Chotana, Photocatalytic degradation of imidacloprid by Ag-ZnO composite, Environ. Sci. Pollut. Res. 25 (2018) 27307–27320, https://doi.org/10.1007/s11356-018-2693-8.
[13] A. Zheng, S. Xie, K. Li, C. Zhang, H. Shi, Performance and mechanism investigation on the enhanced photocatalytic removal of atrazine on S-doped g-C3N4, Chemosphere 347 (2024) 140663, https://doi.org/10.1016/j.chemosphere.2023.140663.
[14] A.S. Saghar Jarollahi, Gholamreza Nabiyouni, Ziba Sorinezami, Synthesis and characterization of Fe3O4/TiO2/Ag magnetic nanocomposite with enhanced photocatalytic activity for methylene blue degradation and modeling by an artificial neural network (ANN), J. Nanostructures. 13 (2023) 359–372, https://doi.org/10.22052/JNS.2023.02.005.
[15] S.J. Rosa Amini, Gholamreza Nabiyouni, Removal of azo dyes pollutants: photo catalyst and magnetic investigation of iron oxide-zinc sulfide nanocomposites, J. Nanostruct. 11 (2021) 95–104, https://doi.org/10.22052/JNS.2021.01.011.
[16] A. Kiani, G. Nabiyouni, S. Masoumi, D. Ghanbari, A novel magnetic MgFe2O4–MgTiO3 perovskite nanocomposite: rapid photo-degradation of toxic dyes under visible irradiation, Composites, Part B 175 (2019) 107080, https://doi.org/10.1016/j.compositesb.2019.107080.
[17] N. Eskandari, G. Nabiyouni, S. Masoumi, D. Ghanbari, Preparation of a new magnetic and photo-catalyst CoFe2O4–SrTiO3 perovskite nanocomposite for photo-degradation of toxic dyes under short time visible irradiation, Composites, Part B 176 (2019) 107343, https://doi.org/10.1016/j.compositesb.2019.107343.
[18] S. Kumar, S.K. Sharma, R.D. Kaushik, L.P. Purohit, Chalcogen-doped zinc oxide nanoparticles for photocatalytic degradation of Rhodamine B under the irradiation of ultraviolet light, Mater. Today Chem. 20 (2021) 100464, https://doi.org/10.1016/j.mtchem.2021.100464.
[19] S. Masoumi, G. Nabiyouni, D. Ghanbari, Photo-degradation of Congored, acid brown and acid violet: photo catalyst and magnetic investigation of CuFe2O4–TiO2–Ag nanocomposites, J. Mater. Sci. Mater. Electron. 27 (2016) 11017–11033, https://doi.org/10.1007/s10854-016-5218-6.
[20] S. Kumar, R.D. Kaushik, L.P. Purohit, Novel ZnO tetrapod-reduced graphene oxide nanocomposites for enhanced photocatalytic degradation of phenolic compounds and MB dye, J. Mol. Liq. 327 (2021) 114814, https://doi.org/10.1016/j.molliq.2020.114814.
[21] S. Kumar, S. Kumar, R.D. Kaushik, L.P. Purohit, ZnO-CdO nanocomposites incorporated with graphene oxide nanosheets for efficient photocatalytic degradation of bisphenol A, thymol blue and ciprofloxacin, J. Hazard Mater. 424 (2022) 127332, https://doi.org/10.1016/j.jhazmat.2021.127332.
[22] S. Kumar, R.D. Kaushik, G.K. Upadhyay, L.P. Purohit, rGO-ZnO nanocomposites as efficient photocatalyst for degradation of 4-BP and DEP using high temperature refluxing method in in-situ condition, J. Hazard Mater. 406 (2021) 124300, https://doi.org/10.1016/j.jhazmat.2020.124300.
[23] S. Kumar, R.D. Kaushik, L.P. Purohit, RGO supported ZnO/SnO2 Z-scheme heterojunctions with enriched ROS production towards enhanced photocatalytic mineralization of phenolic compounds and antibiotics at low temperature, J. Colloid Interface Sci. 632 (2023) 196–215, https://doi.org/10.1016/j.jcis.2022.11.040.
[24] H. Adabavazeh, A. Saljooqi, T. Shamspur, A. Mostafavi, Synthesis of polyaniline decorated with ZnO and CoMoO4 nanoparticles for enhanced photocatalytic degradation of imidacloprid pesticide under visible light, Polyhedron 198 (2021) 115058, https://doi.org/10.1016/j.poly.2021.115058.
[25] S. Ahmadian-Fard-Fini, D. Ghanbari, M. Salavati-Niasari, Photoluminescence carbon dot as a sensor for detecting of Pseudomonas aeruginosa bacteria: hydrothermal synthesis of magnetic hollow NiFe2O4-carbon dots nanocomposite material, Composites, Part B 161 (2019) 564–577, https://doi.org/10.1016/j.compositesb.2018.12.131.
[26] G. Luna-Sanguino, A. Ruíz-Delgado, A. Tolosana-Moranchel, L. Pascual, S. Malato, A. Bahamonde, M. Faraldos, Solar photocatalytic degradation of pesticides over TiO2-rGO nanocomposites at pilot plant scale, Sci. Total Environ. 737 (2020) 140286, https://doi.org/10.1016/j.scitotenv.2020.140286.
[27] N. Verma, T.S. Chundawat, H. Chandra, D. Vaya, An efficient time reductive photocatalytic degradation of carcinogenic dyes by TiO2-GO nanocomposite, Mater. Res. Bull. 158 (2023) 112043, https://doi.org/10.1016/j.materresbull.2022.112043.
[28] F.J. Cano, S. Coste, O. Reyes-Vallejo, M. Makowska-Janusik, S. Velumani, M. de la L. Olvera, A. Kassiba, Influence of GO oxidation degrees on the organization and physical features of TiO2-GO-based nanocomposites for water dye removal, Surface. Interfac. (2024) 104004, https://doi.org/10.1016/j.surfin.2024.104004.
[29] A.B. Migdadi, Q.M. Al-Bataineh, A.A. Ahmad, H.M. Al-Khateeb, A. Telfah, Titanium dioxide/reduced graphene oxide nanocomposites as effective photocatalytic for hazardous 4-nitrophenol, J. Alloys Compd. 971 (2024) 172794, https://doi.org/10.1016/j.jallcom.2023.172794.
[30] A. Naz, I. Bibi, F. Majid, A. Dahshan, K. Jilani, B. Taj, A. Ghafoor, Z. Nazeer, F. M. Alzahrani, M. Iqbal, Cu and Fe doped NiCo2O4/g-C3N4 nanocomposite ferroelectric, magnetic, dielectric and optical properties: visible light-driven photocatalytic degradation of RhB and CR dyes, Diam. Relat. Mater. 141 (2024) 110592, https://doi.org/10.1016/j.diamond.2023.110592.
[31] M. Mohammadi, A. Maleki, S. Zandi, E. Mohammadi, E. Ghahremani, J.-K. Yang, S.-M. Lee, Photocatalytic decomposition of aqueous diazinon using reduced graphene/ZnO nanocomposite doped with manganese, Desalin. WATER Treat. 184 (2020) 315–325, https://doi.org/10.5004/dwt.2020.25392.
[32] P.S. Chauhan, R. Kant, A. Rai, A. Gupta, S. Bhattacharya, Facile synthesis of ZnO/GO nanoflowers over Si substrate for improved photocatalytic decolorization of MB dye and industrial wastewater under solar irradiation, Mater. Sci. Semicond. Process. 89 (2019) 6–17, https://doi.org/10.1016/j.mssp.2018.08.022.

[33] J. Qin, X. Zhang, Y. Xue, N. Kittiwattanothai, P. Kongsittikul, N. Rodthongkum, S. Limpanart, M. Ma, R. Liu, A facile synthesis of nanorods of ZnO/graphene oxide composites with enhanced photocatalytic activity, Appl. Surf. Sci. 321 (2014) 226–232, https://doi.org/10.1016/j.apsusc.2014.10.008.
[34] V. Harish, M.M. Ansari, D. Tewari, A.B. Yadav, N. Sharma, S. Bawarig, M.-L. García-Betancourt, A. Karatutlu, M. Bechelany, A. Barhoum, Cutting-edge advances in tailoring size, shape, and functionality of nanoparticles and nanostructures: a review, J. Taiwan Inst. Chem. Eng. 149 (2023) 105010, https://doi.org/10.1016/j.jtice.2023.105010.
[35] K. Flores, C. Valdes, D. Ramirez, T.M. Eubanks, J. Lopez, C. Hernandez, M. Alcoutlabi, J.G. Parsons, The effect of hybrid zinc oxide/graphene oxide (ZnO/GO) nano-catalysts on the photocatalytic degradation of simazine, Chemosphere 259 (2020) 127414, https://doi.org/10.1016/j.chemosphere.2020.127414.
[36] K.G. Chandrappa, T.V. Venkatesha, K. Vathsala, C. Shivakumara, A hybrid electrochemical–thermal method for the preparation of large ZnO nanoparticles, J. Nanoparticle Res. 12 (2010) 2667–2678, https://doi.org/10.1007/s11051-009-9846-0.
[37] D.A. Giannakoudakis, T.J. Bandosz, Zinc (hydr)oxide/graphite oxide/AuNPs composites: role of surface features in H2S reactive adsorption, J. Colloid Interface Sci. 436 (2014) 296–305, https://doi.org/10.1016/j.jcis.2014.08.046.
[38] M. Goswami, N.C. Adhikary, S. Bhattacharjee, Effect of annealing temperatures on the structural and optical properties of zinc oxide nanoparticles prepared by chemical precipitation method, Optik 158 (2018) 1006–1015, https://doi.org/10.1016/j.ijleo.2017.12.174.
[39] R. Sonkar, N.J. Mondal, B. Boro, M.P. Ghosh, D. Chowdhury, Cu doped ZnO nanoparticles: correlations between tuneable optoelectronic, antioxidant and photocatalytic activities, J. Phys. Chem. Solid. 185 (2024) 111715, https://doi.org/10.1016/j.jpcs.2023.111715.
[40] P. Bindu, S. Thomas, Estimation of lattice strain in ZnO nanoparticles: X-ray peak profile analysis, J. Theor. Appl. Phys. 8 (2014) 123–134, https://doi.org/10.1007/s40094-014-0141-9.
[41] Y. Ding, Y. Liu, S. Niu, W. Wu, Z.L. Wang, Pyroelectric-field driven defects diffusion along c -axis in ZnO nanobelts under high-energy electron beam irradiation, J. Appl. Phys. 116 (2014), https://doi.org/10.1063/1.4898644.
[42] H. Hu, C. Kang, Z. Xiong, Y. Cui, L. Chen, Tunable electronic structure and magnetic characteristics of ZnO monolayer via vacancy defects, and domain/atomic doping, Mater. Today Commun. 36 (2023) 106789, https://doi.org/10.1016/j.mtcomm.2023.106789.
[43] D. Fischer, D. Zagorac, J.C. Schön, Fundamental insight into the formation of the zinc oxide crystal structure, Thin Solid Films 782 (2023) 140017, https://doi.org/10.1016/j.tsf.2023.140017.
[44] Y. Lin, R. Hong, H. Chen, D. Zhang, J. Xu, Green synthesis of ZnO-GO composites for the photocatalytic degradation of methylene blue, J. Nanomater. 2020 (2020) 1–11, https://doi.org/10.1155/2020/4147357.
[45] I. Boukhoubza, M. Khenfouch, M. Achehboune, L. Leontie, A.C. Galca, M. Enculescu, A. Carlescu, M. Guerboub, B.M. Mothudi, A. Jorio, I. Zorkani, Graphene oxide concentration effect on the optoelectronic properties of ZnO/GO nanocomposites, Nanomaterials 10 (2020) 1532, https://doi.org/10.3390/nano10081532.
[46] A. Khorsand Zak, W.H. Abd Majid, M.E. Abrishami, R. Yousefi, X-ray analysis of ZnO nanoparticles by Williamson–Hall and size–strain plot methods, Solid State Sci. 13 (2011) 251–256, https://doi.org/10.1016/j.solidstatesciences.2010.11.024.
[47] A. Kocyigit, R. Topkaya, Structural, optical and magnetic properties of Ni-Co co-doped ZnO thin films, Mater. Res. Express 6 (2019) 096116, https://doi.org/10.1088/2053-1591/ab120a.
[48] D.G. Manouchehr Behzadi, Saghar jarollahi, Maryam Ahsani Irvani, green synthesis and antibacterial activity of silver nanoparticles using dracocephalum moldavica leaves extract, J. Nanostruct. 12 (2022) 1059–1066, https://doi.org/10.22052/JNS.2022.04.026.
[49] K. Upadhyay, S. Thomas, A. Tharayil, R.K. Tamrakar, Green emitting dysprosium-activated SrY2O4 phosphor for tricolour white light-emitting diode application: structural analysis and luminescence behaviour, Chem. Pap. 77 (2023) 7775–7782, https://doi.org/10.1007/s11696-023-03059-w.
[50] Y.T. Prabhu, K.V. Rao, V.S.S. Kumar, B.S. Kumari, X-ray analysis by Williamson-Hall and size-strain plot methods of ZnO nanoparticles with fuel variation, World J. Nano Sci. Eng. 4 (2014) 21–28, https://doi.org/10.4236/wjnse.2014.41004.
[51] P. Rajeswari, S. Dhanuskodi, Microstructural effects of Mn 2+ ions in ZnO nanoparticles, Cryst. Res. Technol. 48 (2013) 589–598, https://doi.org/10.1002/crat.201300102.
[52] A. Khorsand Zak, W.H.A. Majid, M. Ebrahimizadeh Abrishami, R. Yousefi, R. Parvizi, Synthesis, magnetic properties and X-ray analysis of Zn0.97X0.03O nanoparticles (X = Mn, Ni, and Co) using Scherrer and size–strain plot methods, Solid State Sci. 14 (2012) 488–494, https://doi.org/10.1016/j.solidstatesciences.2012.01.019.
[53] D. Nath, F. Singh, R. Das, X-ray diffraction analysis by Williamson-Hall, Halder-Wagner and size-strain plot methods of CdSe nanoparticles- a comparative study, Mater. Chem. Phys. 239 (2020) 122021, https://doi.org/10.1016/j.matchemphys.2019.122021.
[54] G. Leménager, S. Tusseau-Nenez, M. Thiriet, P.-E. Coulon, K. Lahlil, E. Larquet, T. Gacoin, NaYF4 microstructure, beyond their well-shaped morphology, Nanomaterials 9 (2019) 1560, https://doi.org/10.3390/nano9111560.
[55] A. Verma, U. Kumar, P. Chaudhary, B.C. Yadav, Investigation on structural and optical properties of porous SnO2 nanomaterial fabricated by direct liquid injection chemical vapour deposition technique, Solid State Commun. 348–349 (2022) 114723, https://doi.org/10.1016/j.ssc.2022.114723.
[56] A. Bjelajac, I. Florea, M. Zamfir, S.T. Nenez, C.S. Cojocaru, Photocatalytic active ZnO 1−x S x @CNTs heteronanostructures, Nanotechnology 34 (2023) 495704, https://doi.org/10.1088/1361-6528/acf6c8.
[57] M. Yilmaz, Investigation of characteristics of ZnO:Ga nanocrystalline thin films with varying dopant content, Mater. Sci. Semicond. Process. 40 (2015) 99–106, https://doi.org/10.1016/j.mssp.2015.06.031.
[58] S. Debnath, R. Das, Cobalt doping on nickel ferrite nanocrystals enhances the micro-structural and magnetic properties: shows a correlation between them, J. Alloys Compd. 852 (2021) 156884, https://doi.org/10.1016/j.jallcom.2020.156884.
[59] P. Vasudevan, Biogenic synthesis of Cerium oxide nanoparticles using Justicia Adathoda leaves extract: size-strain study by X-ray peak profile analysis and luminescence characteristics, J. Mol. Struct. 1272 (2023) 134144, https://doi.org/10.1016/j.molstruc.2022.134144.
[60] S. Yadav, K. Shrivas, P.K. Bajpai, Role of precursors in controlling the size, shape and morphology in the synthesis of copper sulfide nanoparticles and their application for fluorescence detection, J. Alloys Compd. 772 (2019) 579–592, https://doi.org/10.1016/j.jallcom.2018.08.132.
[61] L. Wang, M. Muhammed, Synthesis of zinc oxide nanoparticles with controlled morphology, J. Mater. Chem. 9 (1999) 2871–2878, https://doi.org/10.1039/a907098b.
[62] A. Azam, F. Ahmed, N. Arshi, M. Chaman, A.H. Naqvi, Formation and characterization of ZnO nanopowder synthesized by sol–gel method, J. Alloys Compd. 496 (2010) 399–402, https://doi.org/10.1016/j.jallcom.2010.02.028.
[63] R. Khokhra, R.K. Singh, R. Kumar, Effect of synthesis medium on aggregation tendencies of ZnO nanosheets and their superior photocatalytic performance, J. Mater. Sci. 50 (2015) 819–832, https://doi.org/10.1007/s10853-014-8642-0.
[64] E.-S. Jeong, I.-H. Hwang, S.-W. Han, Crystallization of transition-metal oxides in aqueous solution beyond Ostwald ripening, Langmuir 36 (2020) 10565–10576, https://doi.org/10.1021/acs.langmuir.0c01903.
[65] L. Liu, M. Ge, H. Liu, C. Guo, Y. Wang, Z. Zhou, Controlled synthesis of ZnO with adjustable morphologies from nanosheets to microspheres, Coll. Surf. Physicochem. Eng. Asp. 348 (2009) 124–129, https://doi.org/10.1016/j.colsurfa.2009.07.003.
[66] R. Shi, P. Yang, X. Song, J. Wang, Q. Che, A. Zhang, ZnO flower: self-assembly growth from nanosheets with exposed {1 1¯ 0 0} facet, white emission, and enhanced photocatalysis, Appl. Surf. Sci. 366 (2016) 506–513, https://doi.org/10.1016/j.apsusc.2016.01.113.
[67] S.W. Kim, N.T. Khoa, J.W. Yun, D. van Thuan, E.J. Kim, S.H. Hahn, Hierarchical ZnO nanosheets/nanodisks hydrothermally grown on microrod backbones, Mater. Chem. Phys. 171 (2016) 252–259, https://doi.org/10.1016/j.matchemphys.2016.01.015.
[68] Y.-L. Chen, C.-E. Zhang, C. Deng, P. Fei, M. Zhong, B.-T. Su, Preparation of ZnO/GO composite material with highly photocatalytic performance via an improved two-step method, Chin. Chem. Lett. 24 (2013) 518–520, https://doi.org/10.1016/j.cclet.2013.03.034.
[69] T. Ivanova, A. Harizanova, T. Koutzarova, B. Vertruyen, Study of ZnO sol–gel films: effect of annealing, Mater. Lett. 64 (2010) 1147–1149, https://doi.org/10.1016/j.matlet.2010.02.033.
[70] K. SinghNancy, M. Bhattu, G. Singh, N.M. Mubarak, J. Singh, Light-absorption-driven photocatalysis and antimicrobial potential of PVP-capped zinc oxide nanoparticles, Sci. Rep. 13 (2023) 13886, https://doi.org/10.1038/s41598-023-41103-7.
[71] U. Vijayalakshmi, M. Chellappa, U. Anjaneyulu, G. Manivasagam, S. Sethu, Influence of coating parameter and sintering atmosphere on the corrosion resistance behavior of electrophoretically deposited composite coatings, Mater. Manuf. Process. 31 (2016) 95–106, https://doi.org/10.1080/10426914.2015.1070424.
[72] D.D. Thongam, J. Gupta, N.K. Sahu, Effect of induced defects on the properties of ZnO nanocrystals: surfactant role and spectroscopic analysis, SN Appl. Sci. 1 (2019) 1030, https://doi.org/10.1007/s42452-019-1058-3.
[73] K.B. Babitha, J. Jani Matilda, A. Peer Mohamed, S. Ananthakumar, Catalytically engineered reduced graphene oxide/ZnO hybrid nanocomposites for the adsorption, photoactivity and selective oil pick-up from aqueous media, RSC Adv. 5 (2015) 50223–50233, https://doi.org/10.1039/C5RA04850H.
[74] Y. Huang, M. Liu, Z. Li, Y. Zeng, S. Liu, Raman spectroscopy study of ZnO-based ceramic films fabricated by novel sol–gel process, Mater. Sci. Eng., B 97 (2003) 111–116, https://doi.org/10.1016/S0921-5107(02)00396-3.
[75] R.P. Wang, G. Xu, P. Jin, Size dependence of electron-phonon coupling in ZnO nanowires, Phys. Rev. B 69 (2004) 113303, https://doi.org/10.1103/PhysRevB.69.113303.
[76] E. Erdogan, C. Eden, N. Canpolat, C. Cirak, M. Yilmaz, Optimizing the structural and photocatalytic performance of Ag-decorated ZnO/Zn(OH) 2 nanoparticles for RhB degradation, Int. J. Appl. Ceram. Technol. (2024), https://doi.org/10.1111/ijac.14675.
[77] M.K. Kavitha, H. John, P. Gopinath, R. Philip, Synthesis of reduced graphene oxide–ZnO hybrid with enhanced optical limiting properties, J. Mater. Chem. C 1 (2013) 3669, https://doi.org/10.1039/c3tc30323c.
[78] P. Yadav, A. Bhaduri, Synthesis of ZnO-Graphene Nanocomposite by Chemical Co-precipitation Method and its Structural Characterizations, 2021 020057, https://doi.org/10.1063/5.0061115.
[79] F. Khurshid, M. Jeyavelan, M.S.L. Hudson, S. Nagarajan, Ag-doped ZnO nanorods embedded reduced graphene oxide nanocomposite for photo-electrochemical applications, R. Soc. Open Sci. 6 (2019) 181764, https://doi.org/10.1098/rsos.181764.

[80] P. Kumari, N. Bahadur, X.A. Conlan, M. Laleh, L. Kong, L.A. O'Dell, L.F. Dumée, A. Merenda, Atomically-thin Schottky-like photo-electrocatalytic cross-flow membrane reactors for ultrafast remediation of persistent organic pollutants, Water Res. 218 (2022) 118519, https://doi.org/10.1016/j.watres.2022.118519.
[81] S. Kumar, R.D. Kaushik, L.P. Purohit, Hetro-nanostructured Se-ZnO sustained with RGO nanosheets for enhanced photocatalytic degradation of p-Chlorophenol, p-Nitrophenol and Methylene blue, Sep. Purif. Technol. 275 (2021) 119219, https://doi.org/10.1016/j.seppur.2021.119219.
[82] L. Tabassam, M.J. Khan, S. Hussain, S.A. Khattak, S.K. Shah, A.S. Bhatti, Structural, optical and antimicrobial characteristics of ZnO green nanoparticles, J. Sol. Gel Sci. Technol. 101 (2022) 401–410, https://doi.org/10.1007/s10971-022-05726-y.
[83] S. Dutta, S. Chattopadhyay, M. Sutradhar, A. Sarkar, M. Chakrabarti, D. Sanyal, D. Jana, Defects and the optical absorption in nanocrystalline ZnO, J. Phys. Condens. Matter 19 (2007) 236218, https://doi.org/10.1088/0953-8984/19/23/236218.
[84] S. Alamdari, M.S. Ghamsari, H. Afarideh, A. Mohammadi, S. Geranmayeh, M. J. Tafreshi, M.H. Ehsani, M.H. Majles ara, Preparation and characterization of GO-ZnO nanocomposite for UV detection application, Opt. Mater. 92 (2019) 243–250, https://doi.org/10.1016/j.optmat.2019.04.041.
[85] P. J, N. Kottam, R. A, Investigation of photocatalytic degradation of crystal violet and its correlation with bandgap in ZnO and ZnO/GO nanohybrid, Inorg. Chem. Commun. 125 (2021) 108460, https://doi.org/10.1016/j.inoche.2021.108460.
[86] Z. Durmus, B.Z. Kurt, A. Durmus, Synthesis and characterization of graphene oxide/zinc oxide (GO/ZnO) nanocomposite and its utilization for photocatalytic degradation of basic fuchsin dye, ChemistrySelect 4 (2019) 271–278, https://doi.org/10.1002/slct.201803635.
[87] H. Moussa, E. Girot, K. Mozet, H. Alem, G. Medjahdi, R. Schneider, ZnO rods/reduced graphene oxide composites prepared via a solvothermal reaction for efficient sunlight-driven photocatalysis, Appl. Catal. B Environ. 185 (2016) 11–21, https://doi.org/10.1016/j.apcatb.2015.12.007.
[88] S.H. Meriam Suhaimy, N. Ghazali, F. Arith, B. Fauzi, Enhanced simazine herbicide degradation by optimized fluoride concentrations in TiO2 nanotubes growth, Optik 212 (2020) 164651, https://doi.org/10.1016/j.ijleo.2020.164651.
[89] S. Meriam Suhaimy, C. Lai, H. Tajuddin, E. Samsudin, M. Johan, Impact of TiO2 nanotubes' morphology on the photocatalytic degradation of simazine pollutant, Materials 11 (2018) 2066, https://doi.org/10.3390/ma11112066.
[90] C. Ashina, N. Pugazhenthiran, P. Sathishkumar, M. Selvaraj, M.A. Assiri, C. Rajasekaran, M.A. Gracia-Pinilla, R.V. Mangalaraja, Ultra-small Ni@NiFe2O4/TiO2 magnetic nanocomposites activated peroxymonosulphate for solar light-driven photocatalytic mineralization of Simazine, J. Environ. Chem. Eng. 11 (2023) 111342, https://doi.org/10.1016/j.jece.2023.111342.
[91] P. Sathishkumar, R.V. Mangalaraja, H.D. Mansilla, M.A. Gracia-Pinilla, S. Anandan, Sonophotocatalytic (42kHz) degradation of Simazine in the presence of Au–TiO2 nanocatalysts, Appl. Catal. B Environ. 160–161 (2014) 692–700, https://doi.org/10.1016/j.apcatb.2014.06.027.
[92] H. Fakhri, M. Farzadkia, R. Boukherroub, V. Srivastava, M. Sillanpää, Design and preparation of core-shell structured magnetic graphene oxide@MIL-101(Fe): photocatalysis under shell to remove diazinon and atrazine pesticides, Sol. Energy 208 (2020) 990–1000, https://doi.org/10.1016/j.solener.2020.08.050.
[93] A. Jonidi-Jafari, M. Shirzad-Siboni, J.-K. Yang, M. Naimi-Joubani, M. Farrokhi, Photocatalytic degradation of diazinon with illuminated ZnO–TiO2 composite, J. Taiwan Inst. Chem. Eng. 50 (2015) 100–107, https://doi.org/10.1016/j.jtice.2014.12.020.
[94] A. Mohagheghian, K. Ayagh, K. Godini, M. Shirzad-Siboni, Using amino-functionalized Fe3O4-WO3 nanoparticles for diazinon removal from synthetic and real water samples in presence of UV irradiation, J. Adv. Oxid. Technol. 20 (2017), https://doi.org/10.1515/jaots-2016-0153.
[95] E.M. Samsudin, S.B. Abd Hamid, J.C. Juan, W.J. Basirun, G. Centi, Synergetic effects in novel hydrogenated F-doped TiO2 photocatalysts, Appl. Surf. Sci. 370 (2016) 380–393, https://doi.org/10.1016/j.apsusc.2016.02.172.
[96] N.T.T. Truc, D.S. Duc, D. Van Thuan, T. Al Tahtamouni, T.-D. Pham, N.T. Hanh, D.T. Tran, M.V. Nguyen, N.M. Dang, N.T.P. Le Chi, V.N. Nguyen, The advanced photocatalytic degradation of atrazine by direct Z-scheme Cu doped ZnO/g-C3N4, Appl. Surf. Sci. 489 (2019) 875–882, https://doi.org/10.1016/j.apsusc.2019.05.360.
[97] T.M. Rünger, U.P. Kappes, Mechanisms of mutation formation with long-wave ultraviolet light (UVA), Photodermatol. Photoimmunol. Photomed. 24 (2008) 2–10, https://doi.org/10.1111/j.1600-0781.2008.00319.x.
[98] H. Sudrajat, S. Babel, I. Thushari, K. Laohhasurayotin, Stability of La dopants in NaTaO3 photocatalysts, J. Alloys Compd. 775 (2019) 1277–1285, https://doi.org/10.1016/j.jallcom.2018.10.237.
[99] D.A. Reddy, J. Choi, S. Lee, Y. Kim, S. Hong, D.P. Kumar, T.K. Kim, Hierarchical dandelion-flower-like cobalt-phosphide modified CdS/reduced graphene oxide-MoS 2 nanocomposites as a noble-metal-free catalyst for efficient hydrogen evolution from water, Catal. Sci. Technol. 6 (2016) 6197–6206, https://doi.org/10.1039/C6CY00768F.
[100] D.S. Sutar, N. Kushwaha, S.K. Appani, S.S. Major, Energy level alignment of graphene oxide and its derivatives with ZnO, J. Electron. Spectrosc. Relat. Phenom. 243 (2020) 146953, https://doi.org/10.1016/j.elspec.2020.146953.
[101] K. Vasanthkumar, K. Porkodi, A. Selvaganapathi, Constrain in solving Langmuir–Hinshelwood kinetic expression for the photocatalytic degradation of Auramine O aqueous solutions by ZnO catalyst, Dyes Pigments 75 (2007) 246–249, https://doi.org/10.1016/j.dyepig.2006.05.035.
[102] S. Chakrabarti, B. Dutta, Photocatalytic degradation of model textile dyes in wastewater using ZnO as semiconductor catalyst, J. Hazard Mater. 112 (2004) 269–278, https://doi.org/10.1016/j.jhazmat.2004.05.013.
[103] S.M. Hassan, M. Farag, S.M. El-Dafrawy, Photodegradation of cationic and anionic dyes by ZnO and S/ZnO biosynthesized nano-photocatalysts, Appl. Organomet. Chem. (2024), https://doi.org/10.1002/aoc.7387.
[104] M.N. Ahmad, M.N. Anjum, M.F. Farid, A. Haq, A. Ali, M.F. Rehman, M.A. Assiri, M.S. Akram, Water pollution remediation: synthesis and characterization of poly (o -methylaniline)/ZnO/rGO composite for photocatalytic degradation of dyes, Polym. Adv. Technol. 35 (2024), https://doi.org/10.1002/pat.6269.
[105] X. Yang, V. Salles, M. Maillard, Y.V. Kaneti, M. Liu, C. Journet, X. Jiang, Y. Liu, A. Brioude, Fabrication of Au functionalized TiO2 nanofibers for photocatalytic application, J. Nanoparticle Res. 21 (2019) 160, https://doi.org/10.1007/s11051-019-4600-8.